THE UNIVERSITY OF CALGARY

Spectral Methods for Post Processing of Airborne Vector Gravity Data

by

Liming Wu

A THESIS

SUBMITTED TO THE FACULTY OF GRADUATE STUDIES

IN PARTIAL FULFILMENT OF THE REQUIREMENTS FOR THE

DEGREE OF MASTER OF SCIENCE IN GEOMATICS ENGINEERING

DEPARTMENT OF GEOMATICS ENGINEERING

CALGARY, ALBERTA

DECEMBER, 1996

ABSTRACT

This thesis deals with the use of spectral methods for the post processing of airborne vector gravity data. In general, two aspects are discussed: 1) filtering and combining airborne measurements for the estimation of gravity disturbance vector components with higher accuracy; 2) the downward continuation of airborne gravity data to a level surface and to an arbitrary surface as well. Two spectral methods, namely input-output system theory and frequency domain least-squares adjustment, are discussed and examined for filtering and combination purposes. Numerical results show that, by filtering and combining all three components of airborne gravity vector rather than filtering one of the components alone, the estimation accuracy will be improved approximately by 10 percent for the vertical component and by 60 percent for the horizontal components within the wavelength range from 10 km to 100 km. In the downward continuation, more stable and accurate results for every component can be expected when it is combined with other components

ACKNOWLEDGEMENT

I wish to express my gratitude to my supervisor, Dr. Michael G. Sideris, for his continuous support, encouragement and constructive criticism throughout the course of my graduate studies. I also wish to express my sincere thanks to Dr. Klaus-Peter Schwarz for being my interim supervisor during the period of Dr. Sideris's sabbatical leave and for his helpful comments on the thesis. Dr. G. Lachapelle and Dr. P. Wu are gratefully acknowledged for their valuable advice on this thesis.

I am grateful to many of my former teachers and colleagues in China but, particularly, to Prof. Zelin Guan and Prof. Chuanhui Zuo, for their continuous guidance and help during the period I was under their supervision. Special thanks are due to Mr. Y. Li, Mr. Z. Li, and Mr. H. Sun for their help in many aspects. Dr. M. Wei is greatly appreciated for helping me with the noise PSD models of airborne gravimetry.

Financial support came from the University of Calgary in the form of Teaching and Research Assistantships, and from the National Sciences and Engineering Research Council of Canada. This is gratefully acknowledged.

Finally, my deepest thanks goes to my wife, Duoyun Yang, for her continuous unconditional support, and to our son, Xu Wu, for sharing the life of a foreign graduate student.

TABLE OF CONTENTS

LIST OF TABLES

LIST OF FIGURES

NOTATIONS

t	time
τ	time interval or delay
ω	time frequency
$X(t)$, $Y(t)$	random signals
$x(t)$, $y(t)$	samples of random signals X(t) and Y(t)
μ_x	mean value of a random signal x
R_{xx}	autocorrelation function of a random signal x
R_{xy}	cross correlation function of random signals x and y
PSD	power spectral density
CPSD	cross power spectral density
Σ	sum
P_{xx}	PSD function of a random signal x
P_{xy}	CPSD function of two random signals x and y
ΔT	sampling rate of a discrete random signal
h_i	impulse response function
H_i	frequency response function
Eq.	equation
γ_{12}	coherence function

T	anomalous gravity potential
W	Earth's gravity potential
U	Earth's normal gravity potential
x	Cartesian coordinate
y	Cartesian coordinate
z	Cartesian coordinate
φ	geodetic latitude
λ	geodetic longitude
ξ, η	deflections of the vertical
ς	height anomaly
δg	gravity disturbance
T_x, T_y, T_z	components of gravity disturbance vector
F	Fourier transform
F^{-1}	inverse Fourier transform
FFT	fast Fourier transform
j	square root of -1
u	spatial frequency in x direction
v	spatial frequency in y direction
q	circular frequency
$*$	convolution operator
superscript *	complex conjugation operator

GPS	global positioning system
INS	inertial survey system
1-D	one-dimensional
2-D	two-dimensional
Min	minimum
Max	maximum
Std. Dev.	standard deviation
σ	standard deviation
G	Newton's gravitational constant
γ	normal gravity
$\rho(x,y)$	point mass

CHAPTER 1

INTRODUCTION

1.1 RESEARCH BACKGROUND

Airborne gravimetry is a very active field of research at the present time. However, most research in this field has been focused on observation techniques rather than on post data processing (Brozena et al., 1989; Kleusberg et al., 1989; Knickmeyer, 1990; Schwarz and Wei, 1994; Schwarz et al., 1994; Schwarz et al., 1991; Wei and Schwarz, 1994; etc.). In addition, few publications deal with the downward continuation of airborne scalar gravimetry data (Schwarz, 1973; Forsberg, 1995; Keller, 1995; etc.). Obviously, there is still a great deal of research to be done on the post processing of airborne gravimetry measurements, especially in the area of airborne vector gravimetry.

In airborne vector gravimetry, all three components of the gravity disturbance vector are measured. However, their accuracies are not the same. Primarily due to the drift of the INS measurements, when the time frequency f decreases, the error spectra of the horizontal components increase as $1/f^4$, while the error spectrum of the vertical component increases as $1/f^2$ (Colombo, 1990; Schwarz and Wei, 1994). As a result, the error in the horizontal components is much greater than the error in the vertical component. However, in some applications such as the determination of the slope of the geoid, the

deflections of the vertical are of more concern. In these cases, more accurate deflections from airborne vector gravimetry are desired. For the vertical component, higher accuracy is also needed for various applications in geodesy, solid earth geophysics, and exploration geophysics (Schwarz et al., 1991). With the development of current observation techniques, higher measurement accuracies certainly can be expected. On the other hand, accuracy improvement may also be achieved by filtering and optimally combining the three components of the airborne gravity disturbance vector in the post data processing stage.

Two major problems have to be overcome in post processing airborne vector gravity data. The first problem is filtering and combination. Because the spectra of the gravity signal and measurement noise are overlapping, a filter needs to be applied to attenuate the noise. Considering that all components of the gravity disturbance vector are linearly correlated, which means that there actually are redundant observations in airborne vector gravimetry, better accuracies for all of the components can be obtained by combining them in an optimal way. The second difficulty to be overcome in post data processing is the downward continuation problem. Observations in airborne gravimetry are made at flying altitude. In some applications, the gravity disturbance will be needed on the surface of the Earth rather than at flying height. Thus, the downward continuation problem becomes an issue to be dealt with.

In principle, least-squares collocation, which has been used in geodesy for decades, can be used to solve these two problems. In practice, though, the use of least-squares collocation

is not advisable. The main problem with least-squares collocation is the need of matrix inversion. When large amounts of data need to be processed, such as in airborne gravimetry, it becomes very inefficient computationally. One of the improvements to least-squares collocation is 'fast' collocation (Heller, 1977; Gray, 1977; Eren, 1980; Bottoni and Barzaghi, 1993). When the observations are gridded, their covariance matrix will be a Toeplitz matrix, provided that the covariance functions of both the gravity signal and the measurement noise depend only on the distance(isotropic). This Toeplitz matrix can be inverted by using FFT techniques. Thus, least-squares collocation can be applied in a much faster way. However, when the number of observations is very large, this method will still be time consuming and inefficient (Eren, 1980). In addition, the two-dimensional covariance function of the measurement noise in airborne gravimetry is not only dependent on the distance but also on direction. Spectral methods are seen as a faster alternative for the post data processing.

Two spectral combination techniques, namely the multiple input-output technique and the frequency domain least-squares adjustment method, are considered as alternatives. A multiple-input single-output system is a system that can combine all the input signals at each frequency (Bendat and Piersol, 1980 and 1986). It employs all the power spectral densities (PSDs) of the input signals and their corresponding noise PSDs to determine the optimum system frequency response. When there is only one input signal, this multiple-input system becomes a Wiener filter. Alternatively, the multiple-input single-output system can be considered as an extension of the Wiener filtering theory. In some literature

(Brown, 1983), the multiple-input single-output system is called the multiple-input Wiener filter. Its formal equivalence to stepwise collocation in the frequency domain has been proven by Sanso and Sideris (1995) and Sideris (1996). The multiple-input system theory has been used successfully for the processing of airborne gradiometry data by Vassiliou (1986). It should also be suitable for the task at hand. However, Vassiliou used only one of the possible approximate solutions in his research. He assumed that noise in all input signals has the same PSD model. This is not the case for airborne vector gravimetry. Hence, an implementation method suitable for airborne vector gravimetry will be studied.

The second spectral combination technique, using the concept of the frequency domain least-squares adjustment method, has been discussed in a number of papers (Barzaghi et al., 1993; Sanso and Sona, 1995). Its use in airborne vector gravimetry data processing was discussed by Sideris (1996) and Wu and Sideris (1995). In this method, the output spectrum corresponding to each of the input signals is computed first. Then all the spectra are combined optimally by applying the least-squares principle as in the spatial domain. The contributing weight for each signal is determined by its noise PSD. Only noise PSDs are required for the frequency domain least-squares adjustment method. Neither of these two spectral combination methods require matrix inversion. With the use of the FFT algorithm, they possess high computational efficiency.

As the covariance function in least-squares collocation, the PSD function is crucial to the spectral combination methods. Two-dimensional noise PSD estimates for airborne vector gravimetry will be necessary for the optimal combination of the components of the airborne gravity disturbance vector. However, thus far, only one-dimensional noise PSD models are available (Wei and Schwarz, 1994; Li and Schwarz, 1994). Theoretically, there is no analytical way to derive the two-dimensional PSD model from a one-dimensional PSD model (Panchev, 1971). In order to effectively research the optimal combination of the components of the airborne gravity disturbance vector, studies on how to practically estimate two-dimensional noise PSDs for airborne vector gravimetry are indispensable.

Besides high computational efficiency, in downward continuation of airborne gravity data, the spectral method has another advantage over least-squares collocation. The spectral downward continuation method uses an analytical approach which is based on Poisson's integral and a series expansion of the gravity field. No a priori information is required for this analytical approach. On the other hand, least-squares collocation is a statistical approach in which a priori information (in the form of covariance functions) plays a key role.

Several airborne scalar gravity surveys were carried out in Greenland, Antartica, and Switzerland (Forsberg and Brozena, 1992; Brozena et al, 1995; Jones et al, 1995; Halliday and Klingele, 1995). The accuracies of their results are in the range of 3-5 mgal

down to wavelengths of 20 km or better. Accuracies of 1-3 mgal over wavelengths of 3-5 km have been achieved in experiments under favourable conditions (Hein, 1995). Typically, the accuracy of airborne scalar gravimetry is currently at about 2-3 mgal down to wavelengths of 10 km. So far, no results of airborne vector gravimetry have been published, although some experiments have been carried out by the Department of Geomatics Engineering at The University of Calgary. Due to the lack of real data, simulated data will be used in this research.

1.2 THESIS OUTLINE

The main objective of the research described in this thesis is to examine the use of spectral techniques in filtering and combination of the airborne gravity disturbance vector components and in the downward continuation of these components. Several practical problems, including the estimation of two-dimensional noise PSDs of airborne gravimetry, the implementation procedure of the multiple-input system for post processing of airborne gravity data, and the accuracy improvement of airborne vector gravimetry with or without noise PSD information, etc., will be addressed.

The thesis consists of six chapters. In Chapter 2, after introducing some basic concepts in signal processing, estimation procedures of the power spectral density of a random signal are reviewed. Then the input-output theory, which is the primary spectral combination

method used in this research, is outlined. In Chapter 3, the relationship between the gravity disturbance vector components in the frequency domain as well as the downward continuation problem of the gradients of the anomalous gravity potential are discussed. In Chapter 4, some practical issues related to the use of spectral techniques in post processing airborne vector gravity data are considered. Also in this chapter, another spectral combination method, the frequency domain least-squares adjustment method, is reviewed. In Chapter 5, numerical tests are conducted to examine the effectiveness of the spectral methods discussed. The results of these tests are presented and analyzed. Finally, in Chapter 6, conclusions and recommendations are given.

CHAPTER 2

FUNDAMENTALS OF SPECTRAL METHODS AND MULTIPLE-INPUT SYSTEM THEORY

This chapter is a review of some basic concepts in signal processing necessary for an understanding of this thesis. The first two sections are about the definition of power spectral density (PSD) and its estimation with fast Fourier transform (FFT) techniques. In Section 3, the concept of the Wiener filter will be introduced. In Section 4, the multiple-input theory will be outlined.

2.1 STATIONARY AND ERGODIC RANDOM SIGNALS

Stationary random signals are commonly used in engineering. If the mean value $\mu_x(t)$ of a random signal X(t) at time t and the autocorrelation function $R_{xx}(t_1,t_2)$ of the same signal at time indices t_1 and t_2 are

$$\begin{aligned} \mu_x(t) &= E\{X(t)\} = \text{const} = \mu_x \\ R_{xx}(t_1,t_2) &= E\{X(t_1)X(t_2)\} = E\{X(t)X(t+\tau)\} = R_{xx}(\tau) \end{aligned} \tag{2.1}$$

this random signal is wide-sense stationary. Eq. (2.1) indicates that the mean value of a wide-sense stationary random signal is constant with respect to time while the corresponding autocorrelation function is only dependent on the interval τ between t_1 and

t_2 , and not on t_1 and t_2 individually. Notice that, here, the expectation operator E is applied to all the samples of the signal X at a particular time.

Another important concept in signal processing is ergodicity. This concept establishes the foundation for the classical methods of power spectral density estimation. As shown in Eq. (2.1), to obtain the mean value and the autocorrelation function, sample averaging is needed. This is rather difficult because, in practice, often only a single sample is available. Thus, it is desirable to estimate all these statistical quantities from one single sample by substituting time averaging for sample averaging. The property required to accomplish this is ergodicity.

If a random signal X(t) is stationary and ergodic, its mean value and autocorrelation function can be defined as

$$\mu_x = \lim_{T\to\infty} \frac{1}{2T} \int_{-T}^{T} x(t)\, dt$$
$$R_{xx} = \lim_{T\to\infty} \frac{1}{2T} \int_{-T}^{T} x(t)x(t+\tau)\, dt \qquad (2.2)$$

where x(t) is a sample of X(t), and T is the half duration of x(t). When there is a joint process of two ergodic random signals X(t) and Y(t), their cross correlation function R_{xy} can be defined as

$$R_{xy} = \lim_{T\to\infty} \frac{1}{2T} \int_{-T}^{T} x(t)y(t+\tau)\, dt \qquad (2.3)$$

where y(t) is a sample of Y(t).

The power spectral density (PSD) P_{xx} of a random signal X(t) is defined as the Fourier transform of the autocorrelation function R_{xx} as follows:

$$P_{xx}(\omega) = \int_{-\infty}^{\infty} R_{xx}(t)\, e^{-j\omega t}\, dt \tag{2.4}$$

$$R_{xx}(t) = \frac{1}{2\pi}\int_{-\pi}^{\pi} P_{xx}(\omega)\, e^{j\omega t}\, d\omega \tag{2.5}$$

where ω is the time frequency and j is the square root of -1. These two equations are known as the Wiener-Khintchine theorem (Cadzow, 1990). The PSD function is always a real positive function.

Similarly, the cross power spectral density (CPSD) P_{xy} of two jointly stationary random signals X(t) and Y(t) is defined as the Fourier transform of their cross correlation function R_{xy}

$$P_{xy}(\omega) = \int_{-\infty}^{\infty} R_{xy}(t)\, e^{-j\omega t}\, dt \tag{2.6}$$

The ergodicity property of a random signal not only permits time average definitions for the mean value and correlation functions, but also permits the equivalent time average definition for the power spectral density functions as follows:

$$P_{xx}(\omega) = \lim_{T\to\infty} \frac{1}{2T}\left|\int_{-T}^{T} x(t)\, e^{-j\omega t}\, dt\right|^2 \tag{2.7}$$

$$P_{xy}(\omega) = \lim_{T\to\infty} \frac{1}{2T}\left[\int_{-T}^{T} x(t)\, e^{-j\omega t}\, dt\right]^*\left[\int_{-T}^{T} y(t)\, e^{-j\omega t}\, dt\right] \tag{2.8}$$

where superscript * denotes the complex conjugate.

2.2 POWER SPECTRAL DENSITY ESTIMATION WITH FFT

PSD estimation is very important in the application of spectral techniques. Numerous modern and classical methods of PSD estimation can be found in signal processing textbooks. Only classical PSD estimation methods will be outlined in this section for two reasons. First, classical methods directly use the PSD definition and are Fourier transform based. FFT techniques can be used to obtain computational efficiency. More importantly, the second reason is that classical methods can be easily extended from one-dimensional cases to multi-dimensional cases. For details about digital spectral analysis, see Marple (1987).

Eq. (2.4) and Eq. (2.7) represent two different definitions for the power spectral density. In practice, signals are sampled discretely at a finite number of points. If the sampling rate $1/\Delta T$ for a signal is constant, the discrete Fourier transform can be used. Eq. (2.4) and Eq. (2.7) then become

$$P_{xx}(k) = \Delta T \sum_{n=0}^{N-1} R_{xx}(n)\, e^{\frac{-j2\pi kn}{N}} \tag{2.9}$$

$$P_{xx}(k) = \frac{1}{N\Delta T}\left|\Delta T \sum_{n=0}^{N-1} x(n)\, e^{\frac{-j2\pi kn}{N}}\right|^2 \tag{2.10}$$

where N is the number of sample points, ΔT is the sampling interval, n is the time index, and k is the frequency index. Similarily, Eq. (2.6) and Eq. (2.8) for the cross power spectral density become

$$P_{xy}(k) = \Delta T \sum_{n=0}^{N-1} R_{xy}(n)\, e^{\frac{-j2\pi kn}{N}} \tag{2.11}$$

$$P_{xy}(k) = \frac{1}{N\Delta T}\left[\Delta T \sum_{n=0}^{N-1} x(n)\, e^{\frac{-j2\pi kn}{N}}\right]^{*}\left[\Delta T \sum_{n=0}^{N-1} y(n)\, e^{\frac{-j2\pi kn}{N}}\right] \tag{2.12}$$

Consequently, there are two types of definition-based methods for PSD estimation. The first type uses Eq. (2.10) and Eq. (2.12) to compute PSD and CPSD directly from the data sample and is called the direct method or periodogram. This method was proposed by Schuster in 1899 (Schuster, 1900). The second type is the indirect method, which must first make an estimate of the correlation, and then Fourier transform it to obtain the PSD estimate. With the advent of FFT algorithms, the direct approach has been widely accepted. The periodogram is used for all the PSD and CPSD estimations in this research.

Due to the finite length of record and the rectangular window effect, using Eq. (2.10) in a direct manner would lead to unsatisfactory results. The standard deviation would be as large as the mean. To improve the quality of periodogram, the following two procedures are recommended in electrical engineering (Bendat and Piersol, 1986; Cadzow, 1990 and Marple, 1987).

Procedure 1:

a. Compute the spectral density function using the whole unwindowed sample.

b. Compute the autocorrelation function by taking the inverse FFT of the PSD estimate.

c. Apply a selected window to the autocorrelation estimate.

d. Take the FFT of the windowed autocorrelation estimate to recompute the smoothed autospectral density function.

e. Adjust the scale factor for the energy loss due to windowing.

Procedure 2:

a. Divide the available data sample into a number of equal length segments half overlapped to adjacent segments.

b. Apply a selected window to each of the segments.

c. Compute a PSD estimate for each segment with FFT.

d. Take the average of all the PSD estimates to obtain the smoothed estimate.

e. Adjust the scale factor for the energy loss due to windowing.

These procedures are also suitable for the cross power spectral density estimation, except that two data samples are involved, so the corresponding formulae for samples should be used. In practice, some data preparation steps, such as data standardization, trend removal, etc., would be included. However, these will not be described here. For details, see Bendat and Piersol (1986). In the case of two-dimensional spectrum analysis, the formulae are formally the same as given in this section. Details can be found in Dudgeon and Mersereau (1984) and Marple (1987).

2.3 THE CONCEPT OF THE WIENER FILTER

In most practical situations, measurements are accompanied by noise. It is necessary to design a filter to extract the signal out of the measurements. If the power spectral densities of the signal and the noise are distributed in different frequency ranges, then the problem is very simple; we just need a low pass, or a high pass, or a band pass filter to eliminate the noise. However, if the power spectral densities of the signal and the noise are overlaping, then the design of a digital filter to eliminate the noise is more complicated. This type of problem was first solved by Norbert Wiener in the early 1940s (Wiener, 1949). The resulting filter is called the Wiener filter.

Assume the measurements $\{x_0(m)\}$ are the sum of a desired signal $\{x(m)\}$ and some noise $\{n(m)\}$. Also assume that both the signal and the noise are stationary random processes and their autocorrelation functions or power spectral densities are known or can be estimated. In this case, the problem can be stated as follows: knowing the power spectral densities of $\{x(m)\}$ and $\{n(m)\}$, design a filter so that if the input of the filter is $\{x(m)+n(m)\}$, the output $\{\hat{x}(m)\}$ will be as close as possible to $\{x(m)\}$. Let h(m) be the unknown impulse response function; then the Wiener filter can expressed as

$$\hat{x}(k) = \sum_{m=-\infty}^{\infty} h(k-m)x_0(m) = \sum_{m=-\infty}^{\infty} h(m)x_0(k-m) \tag{2.13}$$

The optimal h(m) can be determined by minimizing the mean square error

$$e = E\left[(\hat{x}(m) - x(m))^2\right] \tag{2.14}$$

The substitution of Eq. (2.13) into Eq. (2.14) yields

$$e = E\left[\left(\sum_{m=-\infty}^{\infty} h(m)x_0(k-m) - x(k)\right)\left(\sum_{l=-\infty}^{\infty} h(l)x_0(k-l) - x(k)\right)\right]$$

$$= \sum_{m=-\infty}^{\infty}\sum_{l=-\infty}^{\infty} h(m)h(l)E\left[x_0(k-m)x_0(k-l)\right] - 2\sum_{l=-\infty}^{\infty} h(l)E\left[x_0(k-l)x(k)\right] + E\left[x^2(k)\right] \quad (2.15)$$

$$= \sum_{m=-\infty}^{\infty}\sum_{l=-\infty}^{\infty} h(m)h(l)R_{x_0x_0}(m-l) - 2\sum_{l=-\infty}^{\infty} h(l)R_{x_0x}(l) + R_{xx}(0)$$

where $R_{x_0x_0}$ is the autocorrelation function of the measurement $x_0(m)$, R_{xx} is the autocorrelation function of the signal $x(m)$, and R_{x_0x} is the cross correclation function of $x_0(m)$ and $x(m)$. The optimal $h(m)$ must satisfy

$$\frac{\partial e}{\partial h} = 0 \quad (2.16)$$

which implies

$$\sum_{m=-\infty}^{\infty} h(m)R_{x_0x_0}(m-k) = R_{x_0x}(k) \quad (2.17)$$

If the maximum m in Eq. (2.17) is set to a finite number, then by solving the equation, a Wiener FIR (finite impulse response) filter will be obtained. To get a Wiener IIR (infinite impulse response) filter, apply a Fourier transform to Eq. (2.17) and use the definitions of power spectral density and cross power spectral density to obtain

$$H(\omega) = \frac{P_{x_0x}}{P_{x_0x_0}} \quad (2.18)$$

where $H(\omega)$ denotes the frequency reponse of the Wiener IIR filter, $P_{x_0x_0}$ is the power spectral density of the measurements, and P_{x_0x} is the cross power spectral density between the measurement and the true signal.

If we further assume that the true signal and the noise are not correlated to each other, and that P_{xx} and P_{nn} are the power spectral densities of the true signal and the noise, respectively, then Eq. (2.18) becomes

$$H(\omega) = \frac{P_{xx}}{P_{xx} + P_{nn}} \tag{2.19}$$

or

$$H(\omega) = \frac{P_{x_0x_0} - P_{nn}}{P_{x_0x_0}} \tag{2.20}$$

Eq. (2.19) and Eq. (2.20) will be used later in this research. More thorough material about the Wiener filter concept can be found in Cadzow (1989) and Wiener (1949).

2.4 MULTIPLE-INPUT SYSTEM RELATIONSHIPS

It has been mentioned in Chapter 1 that, as an alternative to least square collocation, the multiple-input single-output system may be used for the data processing of airborne vector gravimetry. This section serves as a review of multiple-input system theory from single-

input single-output model to multiple-input multiple-output model. A more detailed discussion can be found in Bendat and Piersol (1986).

2.4.1 Single-Input Single-Output Model

As shown in Figure 2.1, we assume that the input signal x_0 of a single-input single-output system h is stationary and is the sum of the true signal x and some noise n_x. The output signal y_0 of the same system is the joint effect of the desired signal y and the system noise n_y.

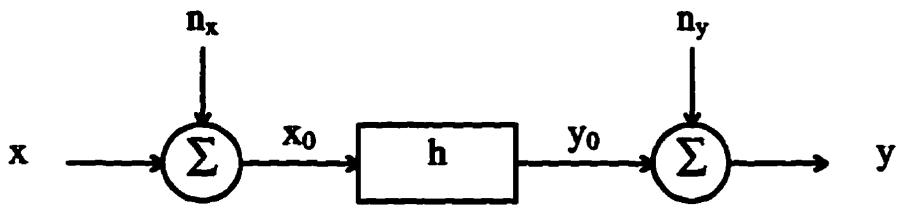

Figure 2.1: A single-input single-output system

Such a system can be expressed mathematically as

$$y = (x + n_x) * h + n_y \tag{2.21}$$

where * denotes the convolution oprator. In the frequency domain, Eq. (2.21) becomes

$$Y = (X + N_x)H + N_y \tag{2.22}$$

where each capital letter stands for the Fourier transform of the sequence denoted by the corresponding lower case letter. The mean square error of the system is

$$E\left[N_y^* N_y\right] = E\left[\left[Y - (X + N_x)H\right]^* \left[Y - (X + N_x)H\right]\right] \tag{2.23}$$

The superscript "*" in this equation means the conjugate of a complex variable. Expanding the term in brakets and applying the expectation operator to the equation lead to the following expression:

$$P_{n_y n_y} = P_{yy} - HP_{yx} - HP_{yn_x} - H^* P_{xy} + H^* HP_{xx} + H^* HP_{xn_x} - H^* P_{n_x y} + H^* HP_{n_x x} + H^* HP_{n_x n_x} \tag{2.24}$$

where all the Ps denote the PSDs and CPSDs of the sequences expressed by their subscript. If we assume that n_x is not correlated with x and y, then their CPSDs are equal to zero and the above equation becomes

$$P_{n_y n_y} = P_{yy} - HP_{yx} - H^* P_{xy} + H^* HP_{xx} + H^* HP_{n_x n_x} \tag{2.25}$$

The optimal frequency response function is the particular H that minimizes $P_{n_y n_y}$ at any frequency, i.e., the one that satisfies

$$\frac{\partial P_{n_y n_y}}{\partial H^*} = 0 \tag{2.26}$$

This leads to the equation

$$-P_{xy} + H(P_{xx} + P_{n_x n_x}) = 0 \tag{2.27}$$

The optimum H is obtained by

$$H = \frac{P_{xy}}{P_{xx} + P_{n_x n_x}} \tag{2.28}$$

The minimized output noise power spectral density is

$$P_{n_y n_y} = P_{yy} - H(P_{xx} + P_{n_x n_x})H^* \tag{2.29}$$

Eq. (2.28) will be identical to Eq. (2.19) if the desired output signal is x itself. Thus, the defined system is essentially equivalent to the Wiener filter. Sideris (1996) showed that such a system is also equivalent to least squares collocation under certain conditions. If there is no input noise, i.e., $P_{n_x n_x} = 0$, Eq. (2.28) represents the frequency response of a ideal single-input single-output system.

2.4.2 Two-Input Single-Output Model

A two-input single-output system is illustrated in Figure 2.2, where x_1 and x_2 are the two input signals, h_1 and h_2 are the impulse responses of the two linear subsystems, y is the system output signal, and n is the system output noise. This system is defined by the following relation in the frequency domain:

$$Y = H_1X_1 + H_2X_2 + N \tag{2.30}$$

Here again, each capital letter stands for the Fourier transform of the sequence denoted by the corresponding lower case letter.

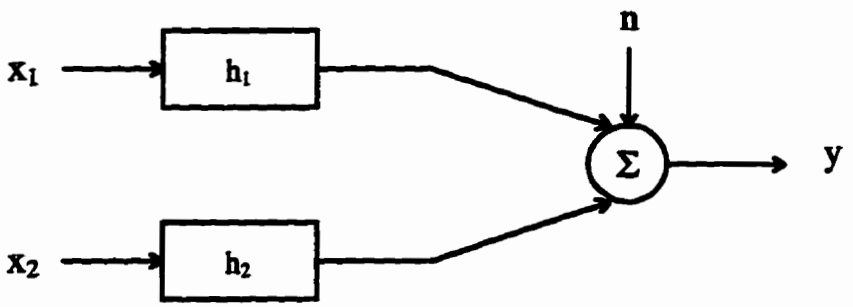

Figure 2.2: A two-input single-output system

The steps to obtain the optimum frequency responses for the two-input system are the same as those for the single-input system. Eq. (2.29) may be rewritten as

$$N = Y - H_1X_1 - H_2X_2 \tag{2.31}$$

Hence, for any H_1 and H_2, the system output noise PSD is

$$\begin{aligned} P_{nn} &= E[N^*N] \\ &= P_{yy} - H_1P_{y1} - H_2P_{y2} - H_1^*P_{1y} + H_1^*H_1P_{11} + H_1^*H_2P_{12} - H_2^*P_{2y} + H_2^*H_1P_{21} + H_2^*H_2P_{22} \end{aligned} \tag{2.32}$$

The optimal frequency response functions are defined as the particular H_1 and H_2 that minimize P_{nn} at any frequency over all possible choices of H_1 and H_2. They yield the optimum linear least squares prediction of y from x_1 and x_2 (Bendat and Piersol, 1986).

To obtain the optimal frequency responses H_1 and H_2, it is sufficient to set the following partial derivatives equal to zero:

$$\frac{\partial P_{nn}}{\partial H_1^*} = 0$$
$$\frac{\partial P_{nn}}{\partial H_2^*} = 0 \qquad (2.33)$$

This leads to

$$-P_{1y} + H_1 P_{11} + H_2 P_{12} = 0$$
$$-P_{2y} + H_1 P_{21} + H_2 P_{22} = 0 \qquad (2.34)$$

The solution to the above equation is given by

$$H_1 = \frac{P_{22}P_{y1} - P_{21}P_{y2}}{P_{11}P_{22} - |P_{12}|^2}$$
$$H_2 = \frac{P_{11}P_{y2} - P_{12}P_{y1}}{P_{11}P_{22} - |P_{12}|^2} \qquad (2.35)$$

or

$$H_1 = \frac{P_{1y}\left(1 - \frac{P_{12}P_{2y}}{P_{22}P_{1y}}\right)}{P_{11}\left(1 - \gamma_{12}^2\right)}$$

$$H_2 = \frac{P_{2y}\left(1 - \frac{P_{21}P_{1y}}{P_{11}P_{2y}}\right)}{P_{22}\left(1-\gamma_{12}^2\right)} \tag{2.36}$$

where γ_{12} is the coherence function.

$$\gamma_{12}^2 = \frac{|P_{12}|^2}{P_{11}P_{22}} \tag{2.37}$$

The minimized output noise power spectral density becomes

$$P_{nn} = P_{yy} - |H_1|^2 P_{11} + H_1^* H_2 P_{12} + H_2^* H_1 P_{21} - |H_2|^2 P_{22} \tag{2.38}$$

Notice that if $P_{11}P_{22}-|P_{12}|^2=0$ or $\gamma_{12}=1$, then the input signals x_1 and x_2 are linearly correlated and the denominators in Eq. (2.35) and Eq. (2.36) are equal to zero. This particular case must be treated separately. Another particular case corresponds to $\gamma_{12}=0$, which indicates that the two inputs are completely uncorrelated. Direct use of Eq. (2.35) or Eq. (2.36) will give incorrect results. These two trivial cases are not of interest here, however, although the components of gravity disturbance vector are linearly correlated, the actual data in airborne vector gravimetry will be only partially correlated because of the existance of measurement noise. For details about these two particular cases, see Sideris (1996) and Bendat and Piersol (1986). For the same reason, when we discuss the multiple-input model, we only consider the case in which the input signals are partially correlated.

2.4.3 Multiple-Input Single-Output Model

If more than two input signals exist, the system is a multiple-input system. Figure 2.3 shows a multiple-input single-output system. A number of q stationary signals x_i (i=1,2,...,q) go through q linear systems with impulse response functions h_i (i=1,2,...,q). Then the outputs of the linear systems are combined together to produce a single output y. n represents the system noise.

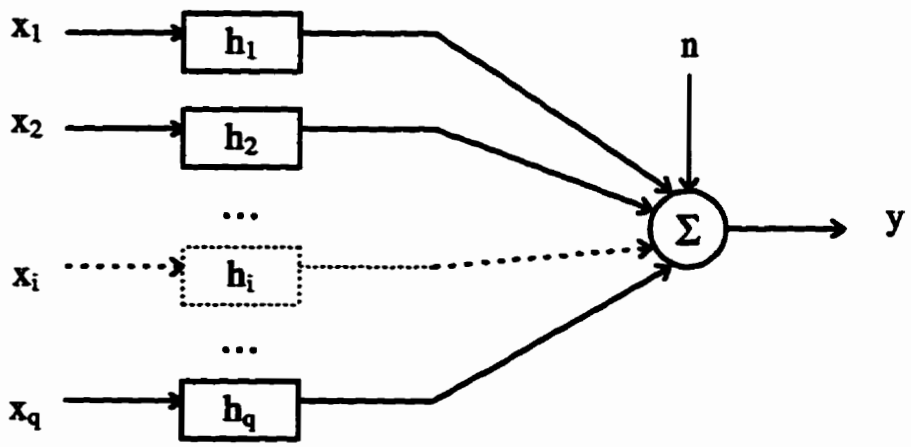

Figure 2.3: A multiple-input single-output system

The equations for this system in the frequency domain are

$$\mathbf{Y} = \sum_{i=1}^{q} \mathbf{H}_i \mathbf{X}_i + \mathbf{N} \tag{2.39}$$

$$N = Y - \sum_{i=1}^{q} H_i X_i \tag{2.40}$$

$$\begin{aligned} P_{nn} &= E[N^* N] \\ &= E\left[\left(Y - \sum_{i=1}^{q} H_i X_i\right)^* \left(Y - \sum_{i=1}^{q} H_i X_i\right)\right] \end{aligned} \tag{2.41}$$

Theoretically, by minimizing the system output noise PSD P_{nn}, we can obtain the optimum frequency response functions H_i, i=1,2,...,q. But, as it can be seen from Eq. (2.41), the whole procedure will be cumbersome if q is a number greater than 2. In addition, very large amounts of memory will be required if a multiple-input system is realized on a computer using the above algorithm. Thus, it is not advisable to use this in practice. A much easier and more efficient procedure will be discussed later in Chapter 4.

2.4.4 Multiple-Input Multiple-Output Model

The multiple-input multiple-output model represents the general case. Let X_i, i=1,2,...,p stand for the Fourier transforms of the p input signals. Y_k, N_k, k=1,2,...,q are the Fourier transforms of the q output signals and their noise. A multiple-input multiple-output system can be expressed as

$$\begin{bmatrix} Y_1 \\ Y_2 \\ \vdots \\ Y_q \end{bmatrix} = \begin{bmatrix} H_{1y1} & H_{2y1} & \cdots & H_{py1} \\ H_{1y2} & H_{2y2} & \cdots & H_{py2} \\ \vdots & \vdots & & \vdots \\ H_{1yq} & H_{2yq} & \cdots & H_{pyq} \end{bmatrix} \begin{bmatrix} X_1 \\ X_2 \\ \vdots \\ X_p \end{bmatrix} + \begin{bmatrix} N_1 \\ N_2 \\ \vdots \\ N_q \end{bmatrix} \tag{2.42}$$

The first matrix on the right hand side is the system frequency response matrix. This equation is equivalent to the following algebraic expression

$$Y_k = \sum_{i=1}^{p} H_{iy_k} X_i + N_k \qquad k = 1,2,...,q \tag{2.43}$$

The above equation has the same form as Eq. (2.39). This means that the multiple-input multiple-output system is an assemblage of a number of q multiple-input single-output systems. Bendat and Piersol (1986) recommended that it be broken down into multiple-input single-output problems and solveld by algebraic procedures.

CHAPTER 3

GRAVITY FIELD MODELING IN THE FREQUENCY DOMAIN

In this chapter, after a very brief review of the concept of the gravity disturbance, the estimation of the PSDs and CPSDs for gravity disturbance components is outlined. In Section 3 of this chapter, the downward continuation problem of airborne gravity disturbance vectors is discussed.

3.1 GRAVITY DISTURBANCE VECTOR AND ITS FOURIER TRANSFORM

Assume W is the gravity potential of the actual Earth and U is the gravity potential of a best fitting ellipsoid, i.e., the normal potential. Then, the anomalous gravity potential T, at a point P, is defined as the difference between W and U at this point (Heiskanen and Moritz, 1967). That is,

$$T(P)=W(P)-U(P) \tag{3.1}$$

The gravity disturbance vector is defined as

$$\delta\bar{g}=\begin{pmatrix} \frac{1}{r}\frac{\partial T}{\partial \varphi} \\ \frac{1}{r\cos\varphi}\frac{\partial T}{\partial \lambda} \\ \frac{\partial T}{\partial r} \end{pmatrix} \tag{3.2}$$

where φ and λ are the geodetic latitude and longitude of P, and r is the distance from the mass centre of the Earth to P.

For local gravity field modeling, the planar approximation is usually introduced. A tangent plane at P is substituted for the ellipsoid surface. The local Cartesian coordinate system is defined as follows: the x-axis points east, the y-axis points north, the z-axis points to the zenith to complete a right-handed rectangular coordinate system. In this coordinate system, the gravity disturbance vector is expressed as

$$\delta\bar{g} = \begin{pmatrix} \frac{\partial T}{\partial y} \\ \frac{\partial T}{\partial x} \\ \frac{\partial T}{\partial z} \end{pmatrix} \tag{3.3}$$

The deflections of the vertical (ξ and η) and the height anomaly (or the geoid undulation) ζ are linked to the anomalous gravity potential by

$$\begin{aligned} \xi &= -\frac{1}{\gamma}\frac{\partial T}{\partial y} \\ \eta &= -\frac{1}{\gamma}\frac{\partial T}{\partial x} \\ \zeta &= \frac{T}{\gamma} \end{aligned} \tag{3.4}$$

For the sake of convenience, we denote $\frac{\partial T}{\partial x}$, $\frac{\partial T}{\partial y}$, and $\frac{\partial T}{\partial z}$ as T_x, T_y, and T_z, respectively.

By using the well-known properties of the two-dimensional Fourier transform, the relations between the components of the gravity disturbance vector and the anomalous potential in the frequency domain can be obtained. In planar approximation, they are:

$$F\{T_x\}=j2\pi uF\{T\}$$

$$F\{T_y\}=j2\pi vF\{T\} \qquad (3.5)$$

$$F\{T_z\}=-2\pi qF\{T\}$$

where F indicates a Fourier transform, u and v are frequencies in the x and y directions, and $q=(u^2+v^2)^{1/2}$. The detailed derivation for these expressions can be found in Sideris (1987) and it is based on the fact that T is a harmonic function.

3.2 PSDs AND CPSDs OF GRAVITY DISTURBANCE COMPONENTS

Power spectral density functions and cross power spectral density functions of the inputs and outputs play a very important role in the implementation of a multiple-input system. In this section, all the PSDs and CPSDs of components of the gravity disturbance vector will be expressed as functions of the PSD of the anomalous gravity potential.

According to the PSD definition given by Eq.(2.7), the PSD of the vertical component is

$$P_{T_zT_z} = \lim_{S\to\infty}\frac{1}{S}\left[F\{T_z\}\right]^* F\{T_z\} \qquad (3.6)$$

where s is the record length. Substituting Eq. (3.5) into the above equation yields

$$P_{T_zT_z} = \lim_{s\to\infty}\frac{1}{S}\left[-2\pi qF\{T\}\right]^{*}F\{-2\pi qT\}$$

$$= 4\pi^2q^2\lim_{s\to\infty}\frac{1}{S}\left[F\{T\}\right]^{*}F\{T\} \qquad (3.7)$$

$$= 4\pi^2q^2P_{TT}$$

where P_{TT} is the PSD of the anomalous gravity potential. By using the PSD definition given by Eq. (2.7), we assume that the gravity disturbance signal is a stationary and ergodic random signal. By using the same definition, the PSDs of the two horizontal components can be derived. They are

$$P_{T_xT_x} = 4\pi^2u^2P_{TT} \qquad (3.8)$$

$$P_{T_yT_y} = 4\pi^2v^2P_{TT} \qquad (3.9)$$

Similarly, with the CPSD definition expressed by Eq. (2.8), the CPSDs of the gravity disturbance vector components can be obtained as follows:

$$P_{T_xT_y} = 4\pi^2uvP_{TT} \qquad (3.10)$$

$$P_{T_xT_z} = -j4\pi^2uqP_{TT} \qquad (3.11)$$

$$P_{T_yT_z} = -j4\pi^2vqP_{TT} \qquad (3.12)$$

Here, only three CPSD functions are given, others can easily be obtained by using the properties of PSD functions. For example, $\left[P_{T_xT_z}\right]^{*} = P_{T_xT_z}$.

Equations (3.7) to (3.12) indicate that all the PSDs and CPSDs are functions of the PSD of the anomalous gravity potential. Thus, if the PSD of the anomalous gravity potential is estimated, all the PSDs and CPSDs of the gravity disturbance vector components are determined. Vassiliou and Schwarz (1985), after numerically analyzing gravity anomalies from sixteen Canadian areas, recommend the following PSD model for the anomalous gravity potential at medium and high frequencies:

$$P_{TT} = \frac{A}{q^{4.6}} \tag{3.13}$$

where A is a scale factor.

3.3 DOWNWARD CONTINUATION OF AIRBORNE GRAVITY DATA

It is necessary for geodetic applications that the airborne gravity measurements be propagated downward to the geoid (for solving Stokes' problem) or to the surface of the Earth (for solving Molodensky's problem). This implies two different types of downward continuation. One is downward continuation to an equal height surface (level surface). The other is downward continuation to an arbitrary surface (e.g., the Earth's surface). These two types of downward continuation will be dealt with separately in this section.

3.3.1 Downward Continuation to a Level Surface

As shown in Figure 3.1, if the value of a harmonic function on the surface V_R is known, the harmonic function outside the surface can be determined by solving the first boundary value problem of physical geodesy (the Dirichlet problem). Furthermore, if the surface is a sphere, the result at point P is given by Poisson's integral (Heiskanen and Moritz, 1967):

$$V_P = \frac{R(r^2 - R^2)}{4\pi} \iint_{\sigma} \frac{1}{l^3} V_R d\sigma \tag{3.14}$$

$$l = \left(R^2 + r^2 - 2Rr\cos\psi\right)^{\frac{1}{2}} \tag{3.15}$$

where σ is the unit sphere correspondent to S. All other quantities are as illustrated in Figure 3.1.

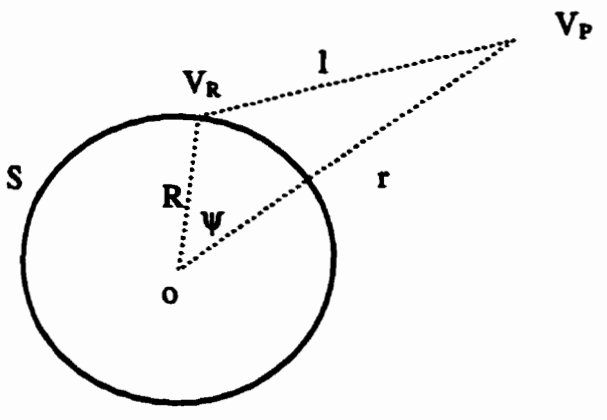

Figure 3.1: The Dirichlet problem

Using curvilinear coordinates, we can rewrite Eq. (3.14) as

$$V_P(\varphi_p,\lambda_p) = \frac{R(r^2-R^2)}{4\pi}\iint_\sigma \frac{1}{l^3} V_R(\varphi,\lambda)\sin\varphi d\varphi d\lambda \tag{3.16}$$

Obviously, Poisson's integral can be used directly in the upward continuation application. It is a convolution integral and is therefore suitable for treatment by FFT techniques (Schwarz et al., 1990). For the upward continuation from one spherical surface to another, we have

$$V_r(\varphi,\lambda) = C\left[K(\varphi,\lambda) * (V_R(\varphi,\lambda)\sin\varphi)\right] \tag{3.17}$$

where $C = \frac{R(r^2-R^2)}{4\pi}$, * denotes the convolution operator, V_R is the harmonic function on the sphere with radius R, V_r is the harmonic function on the sphere with radius r (r > R), and K is the integral kernel correspondent to $1/l^3$. In the frequency domain, this equation becomes

$$F\{V_r(\varphi,\lambda)\} = CF\{K(\varphi,\lambda)\}F\{V_R(\varphi,\lambda)\sin\varphi\} \tag{3.18}$$

where F denotes the 2-D Fourier transform.

For downward continuation, i.e., to obtain V_R from V_r, we have to do deconvolution. It can be easily done in the frequency domain. From Eq. (3.18), we have

$$F\{V_R(\varphi,\lambda)\sin\varphi\} = \frac{1}{C}\frac{F\{V_r(\varphi,\lambda)\}}{F\{K(\varphi,\lambda)\}} \tag{3.19}$$

or

$$V_R(\varphi,\lambda) = \frac{1}{C\sin\varphi} F^{-1}\left\{\frac{F\{V_r(\varphi,\lambda)\}}{F\{K(\varphi,\lambda)\}}\right\} \tag{3.20}$$

where F^{-1} is the 2-D inverse Fourier transform.

The kernel of Poisson's integral decreases very fast with l. For applications in a local area, a planar approximation may be introduced. The planar form of Poisson's integral is

$$V_p(x_p,y_p) = \frac{1}{2\pi}\int\int \frac{z-z_p}{\left((x-x_p)^2+(y-y_p)^2+(z-z_p)^2\right)^{3/2}} V_R(x,y)dxdy \tag{3.21}$$

or

$$V_p(x_p,y_p) = \frac{1}{2\pi}\int\int \frac{H}{\left((x-x_p)^2+(y-y_p)^2+H^2\right)^{3/2}} V_R(x,y)dxdy \tag{3.22}$$

where H is the distance from the surface to the point P, and x, y, and z are coordinates in the local Cartesian coordinate system. Let

$$K(x,y) = \frac{1}{2\pi}\frac{H}{\left(x+y^2+H^2\right)^{3/2}} \tag{3.23}$$

The formula for upward continuation from one level surface to another can be written as

$$V_r(x,y) = K(x,y) * V_R(x,y) \tag{3.24}$$

Kernel K has the analytical spectrum of (Bracewell, 1978)

$$F\{K(x,y)\} = e^{-2\pi Hq} \tag{3.25}$$

where $q=(u^2+v^2)^{\frac{1}{2}}$.

Hence, in the frequency domain, Eq. (3.24) becomes

$$F\{V_r(x,y)\} = e^{-2\pi Hq} F\{V_R(x,y)\} \tag{3.26}$$

Next, the formula for downward continuation from one level surface to another is obtained:

$$F\{V_R(x,y)\} = e^{2\pi Hq} F\{V_r(x,y)\} \tag{3.27}$$

Eq. (3.26) and Eq. (3.27) are very simple. It will be shown in the following chapter that they can be readily used in a multiple-input system to combine gravimetry data on several different level surfaces.

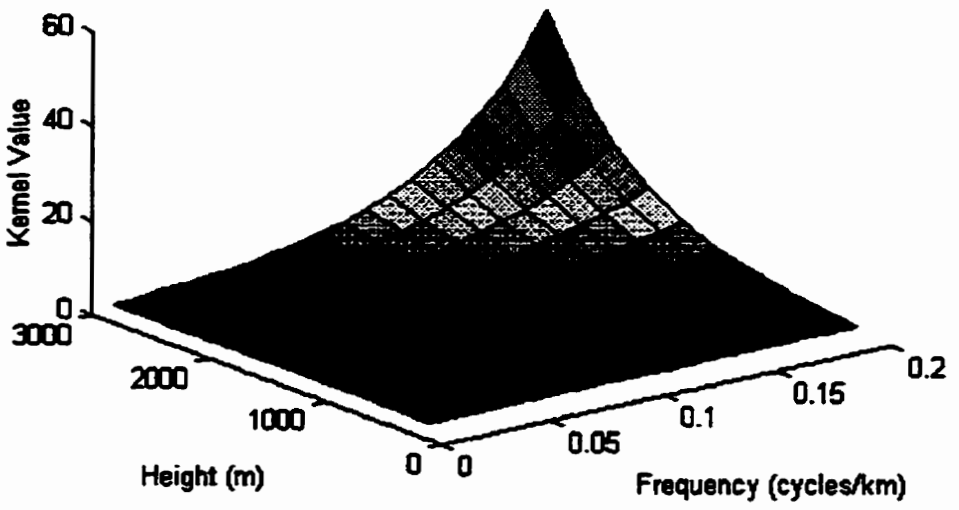

Figure 3.2: Change of downward continuation kernel with height and frequency

It should be pointed out that, in Eq. (3.27), for any $q > 0$, $H > 0$, the downward continuation kernel $e^{2\pi Hq}$ will be greater than unity and will increase with both q and H, as shown in Figure 3.2. This implies that downward continuation is instable, especially at high frequencies. Hence, in the downward continuation of airborne observations, the control of high frequency noise is a critical issue.

So far, we have obtained all expressions for upward and downward continuation of a harmonic function. The question is: can they be applied to the continuation of the gravity disturbance vector components? To answer this, we need to see if the components of the gravity disturbance vector are harmonic functions. From the theory of physical geodesy, we know that the anomalous gravity potential is a harmonic function outside the Earth (if the mass of the atmosphere is neglected). That is

$$\Delta T = 0 \tag{3.28}$$

where Δ denotes the Laplace operator. Taking the vertical component as an example,

$$\Delta T_z = \Delta\left(\frac{\partial T}{\partial z}\right) \tag{3.29}$$

Changing the order of the partial derivative and the Laplace operator in the above equation, we obtain

$$\Delta T_z = \frac{\partial}{\partial z}(\Delta T) = 0 \tag{3.30}$$

Thus, T_z is a harmonic function. Using the same principles, it can be proven that the other two components of the gravity disturbance vector (in fact, all the gradients, or derivatives,

of the anomalous gravity potential) are harmonic functions. This conclusion is based on the harmonic property of the anomalous gravity potential. This means that the mass of the topography has to be taken into consideration, as well.

3.3.2 Downward Continuation to the Surface of the Earth

With the frequency domain convolution and deconvolution techniques, as shown in the previous section, Poisson's integral can be easily used in the downward or upward continuation of airborne gravimetry data from one level surface to another. If values on the Earth's irregular surface are needed, additional procedures should be considered. As shown in Figure 3.3, a Taylor series expansion may be used to obtain values on the Earth's surface from values on the chosen level surface.

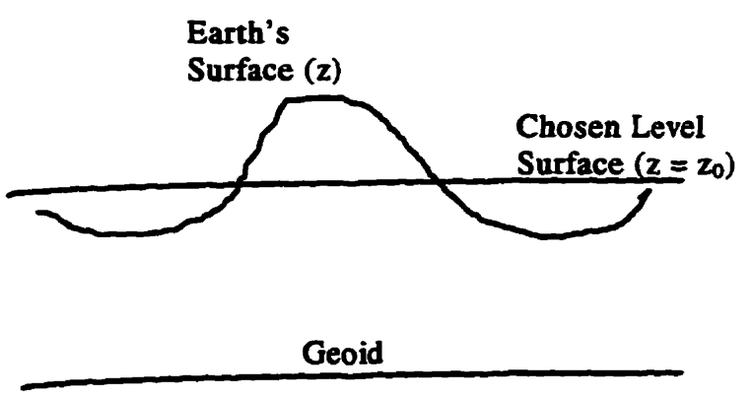

Figure 3.3: Continuation from a chosen level surface to the Earth's surface

The Taylor expansion is

$$V(x,y,z) = V(x,y,z_0) + (z-z_0)\frac{\partial V(x,y,z_0)}{\partial z} + \frac{1}{2!}(z-z_0)^2\frac{\partial^2 V(x,y,z_0)}{\partial z^2} + \frac{1}{3!}(z-z_0)^3\frac{\partial^3 V(x,y,z_0)}{\partial z^3} + \cdots \tag{3.31}$$

where the function V(x,y,z) could be any of the gravity vector components. This equation holds only when all the partial derivatives of V(x,y,z) are continuous. If the chosen level surface is intersected with the topography, as shown in Figure 3.3, the topographic masses must have been removed in advance.

The derivatives in Eq. (3.31) require very large integration computations at each point for the space domain method (Moritz,1980). However, this can be avoided by using the spectral method (Sideris, 1987). The Fourier transform of the r^{th} vertical derivative of any gravimetric harmonic function V(x,y) is given by

$$F\left\{\frac{\partial^r V(x,y)}{\partial z^r}\right\} = (-2\pi q)^r F\{V(x,y)\} \tag{3.32}$$

Notice that F{V(x,y)} can be obtained with the methods discussed in the previous section, which can be built into the multiple-input system or other frequency domain combination methods. Thus, the r^{th} derivative of V(x,y) can be computed very easily as a by-product of those combination methods.

Choosing an optimal z_0 will help to reduce the higher order term effect in Eq. (3.31). z_0 should be chosen in such a way that $(z-z_0)$ has a minimum variation. Hence, z_0 should be

the mean value of z. This implies that a remove-restore procedure of the topography will be involved. Spectral methods for the computations of terrain effects on a level surface and the Earth's surface have become well-researched over the past decade (Parker 1972; Sideris 1984, 1990; Forsberg 1985; Sideris and Tziavos 1988; Tziavos et al. 1988).

In most cases, the computation of the first-order term in Eq. (3.31) should be enough. The consideration of the second-order term might be needed if the gravity field is extremely rugged.

The procedure for downward continuation of the airborne gravity disturbance vector is:

1. Remove the topography effect from the gravity vector at flight level;
2. Downward continue all gravity components to the average topographic height;
3. Propagate the components to the Earth's irregular surface with Eq. (3.31);
4. Restore the topography effect at each point on the Earth's surface.

CHAPTER 4

PROCESSING OF AIRBORNE VECTOR GRAVITY DATA WITH SPECTRAL TECHNIQUES

This chapter deals with some practical aspects of spectral techniques used for airborne gravity data processing. The first section is a numerical investigation into the two-dimensional noise PSD of airborne gravimetry. Special consideration is given to the effect of the flight route pattern. In the second section, the implementation of the multiple-input single-output system for airborne vector gravimetry is discussed. A procedure is proposed to reduce the computer memory requirement as well as the computational work. In the third section, the frequency domain least-squares adjustment method is briefly introduced and examined for its use in airborne vector gravity data processing. Finally, in the fourth section, some special cases regarding the combination of gravity data at different level surfaces and accuracy improvements of airborne gravity data when no error PSD information is available are discussed.

4.1 ANALYSIS OF TWO-DIMENSIONAL NOISE PSD OF AIRBORNE GRAVIMETRY

In this section, an existing one-dimensional noise PSD model of airborne vector gravimetry will be briefly described first. Then a numerical approach for estimating two-dimension PSD from the one-dimensional PSD model will be outlined and used to analyze two-dimensional noise PSD of airborne vector gravimetry.

4.1.1 One-Dimensional Noise PSDs of Airborne Vector Gravimetry

There are three different types of airborne gravimetry system: i> Damped two-axes platform system, e.g., Lacoste & Romberg sea/air gravity meter system; ii> Schuler-tuned three axes platform system; iii> Strapdown inertial navigation system(Hein, 1995). Error models used in this research are only suitable for the third type of system. For other types of systems, different error models should be considered.

The one-dimensional (1-D) noise PSD models for INS and GPS can be found in Schwarz et al. (1994) and Schwarz and Wei (1994). They are given directly here. For details, these two papers should be consulted. The 1-D noise PSD model for INS measured specific force in the horizontal channels is

$$P_{ff}(\omega) = \frac{g^2}{R^2}\frac{1}{\omega^2(\omega^2-\omega_s^2)^2}b_a^2 + \frac{g^2}{(\omega^2-\omega_s^2)^2}d_g^2 + \frac{2\beta_a}{\omega^2+\beta_a^2}\sigma_a^2 + Q_a \qquad (4.1)$$

where b_a^2 is the PSD of the constant accelerometer bias, d_g^2 is the PSD of gyro drift, σ_a^2 is the variance of accelerometer colored noise, Q_a is the PSD of white noise, ω_s is the Schuler frequency, and β_a is the inverse of the correlation time of accelerometer colored noise.

In the 1-D error PSD model of the vertical channel, the constant accelerometer bias term and the gyro drift term become negligible so that the model can be written as

$$P_{ff}(\omega) = \frac{2\beta_a}{\omega^2 + \beta_a^2}\sigma_a^2 + Q_a \tag{4.2}$$

The 1-D error model for GPS measured acceleration is provided by Schwarz and Wei (1994) as follows:

$$P_{gg}(\omega) = \omega^4 \frac{2\beta_g}{\omega^2 + \beta_g^2}\sigma_g^2 + \omega^4 Q_g \tag{4.3}$$

where σ_g^2 is the variance of the correlated GPS position errors, β_g is the inverse of the correlation time, and Q_g is the PSD of the white noise in GPS positioning.

The 1-D error PSD of airborne gravity data is the sum of the PSDs of the INS measured specific error and the GPS measured acceleration error. For the horizontal channel, we have

$$P_{hh}(\omega) = \frac{g^2}{(\omega^2 - \omega_s^2)^2} d_g^2 + \frac{2\beta_a}{\omega^2 + \beta_a^2}\sigma_a^2 + Q_a + \omega^4 \frac{2\beta_g}{\omega^2 + \beta_g^2}\sigma_g^2 + \omega^4 Q_g \tag{4.4}$$

For the vertical channel, we have

$$P_{vv}(\omega) = \frac{2\beta_a}{\omega^2+\beta_a^2}\sigma_a^2 + Q_a + \omega^4\frac{2\beta_g}{\omega^2+\beta_g^2}\sigma_g^2 + \omega^4 Q_g \qquad (4.5)$$

In Eq. (4.4) and Eq.(4.5), each term corresponds to a particular error source. There is no cross PSD term in these two equations. This means that the assumption has been made that the error sources are not correlated to each other. Due to aircraft dynamics, this assumption is not true, especially in the high frequency band. But, considering that the simulation study will be restricted to geodetic application where relatively low frequencies of the gravity signal have to be estimated, the assumption may not affect final results significantly. For the sake of simplicit, these simple PSD models will be used in this research.

Table 4.1: Parameter Values Used for Noise PSD Models

Parameter	*Value*
b_a	10 mgal/$\sqrt{\text{Hz}}$
d_g	10^{-3} deg/h/$\sqrt{\text{Hz}}$
σ_a	10 mgal
Q_a	1 mgal/$\sqrt{\text{Hz}}$
$1/\beta_a$	2 h
σ_g	0.03 m
Q_q	0.005 m
$1/\beta_g$	1000 sec

The parameter values for the PSD models used in this research are taken from Schwarz et al. (1994) and Schwarz and Wei (1994). They are listed in Table 4.1.

Figure 4.1 shows the 1-D error PSDs of the horizontal components and the vertical component of the airborne gravity disturbance vector within the frequency band from $5x10^{-4}$ Hz to $1x10^{-1}$ Hz. The frequency band corresponds to the wavelength range from 111.11 km to 0.56 km if the aircraft velocity is assumed to be 200 km/h.

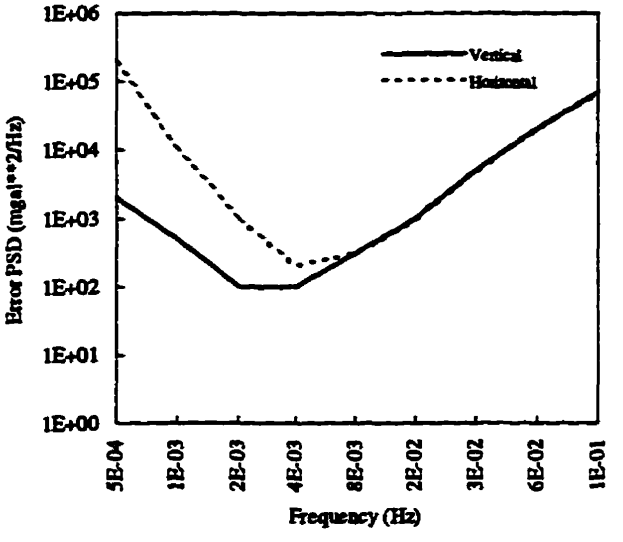

Figure 4.1: 1-D noise PSD of airborne vector gravimetry

4.1.2 Estimate Two-Dimensional Noise PSD With a Numerical Approach

Two-dimensional (2-D) noise PSD information is indispensable for the implementation of the multiple-input system for airborne vector gravimetry. However, a general analytical 2-

D noise PSD model for airborne gravimetry cannot be derived because the form of such a model would be strongly affected by the flight route pattern. In this section, the 2-D noise PSD for a typical pattern, i.e. one in which the flight routes are parallel lines, will be examined numerically with the methods discussed in Chapter 2. Two special cases will be considered. In case (1), the area is covered by a number of independent flights. In case (2), the area is covered by a single flight. These two cases are illustrated in Figure 4.2.

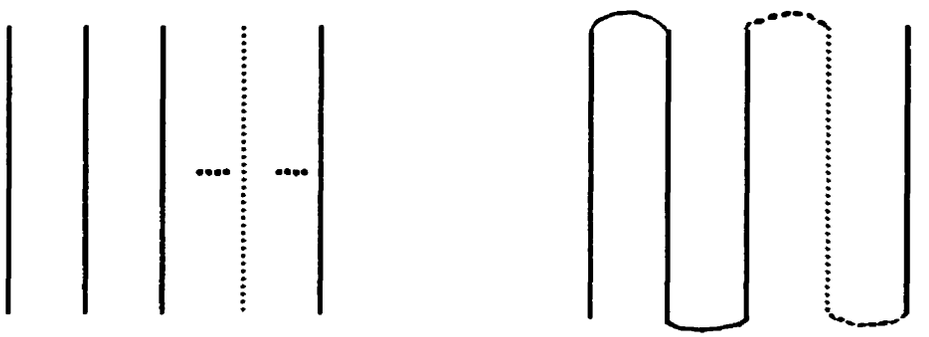

Figure 4.2: Illustration of the two cases: (1) Area is covered by a number of independent flights in the same direction; (2) Area is covered by a single flight

To estimate the 2-D noise PSDs, noise for each case illustrated in Figure 4.2 is simulated using the spectral scaling technique. As illustrated in Figure 4.3, the spectral scaling technique consists of two parts. One is a random noise generator and the other is a low pass filter used for scaling the PSD of the output to the desired one. Because of its function, this low pass filter will be called the power spectral density shaping filter.

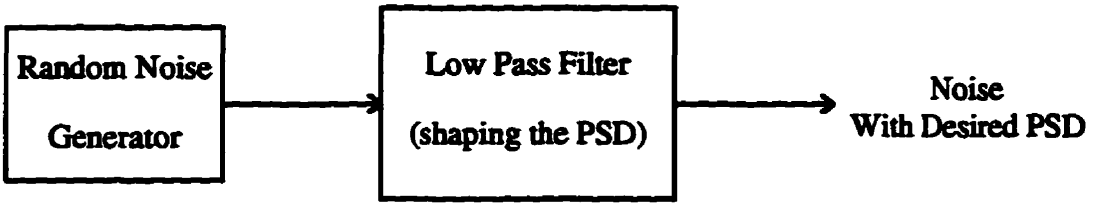

Figure 4.3: Noise simulation by spectrum scaling technique

The design of the power spectral density shaping filter is simple. Assume that x(t) is the noise series generated by the random noise generator, $g_{yx}(t)$ is the impulse response function of the filter to be designed and y(t) is the output of the filter. In the frequency domain we have

$$Y(\omega) = G_{yx}(\omega)X(\omega) \tag{4.6}$$

where $X(\omega)$, $G_{yx}(\omega)$, $Y(\omega)$ are the Fourier transform of x(t), $g_{yx}(t)$, y(t), respectively. Then we also have

$$P_{yy}(\omega) = G_{yx}(\omega)G^{*}_{yx}(\omega)P_{xx}(\omega) \tag{4.7}$$

where P_{xx} and P_{yy} are the power spectral densities of x(t) and y(t). Usually, P_{xx} and P_{yy} are considered to be known. By choosing any G_{yx} that satisfies Eq. (4.7), we can obtain the resulting power spectral density shaping filter.

For that each term in Eq. (4.4) and Eq. (4.5) is the PSD of an independent error source, each type of errors can be simulated separately and added together to the total error of

airborne gravimetry. Assuming that the random noise generator generates a white noise sequence with unity PSD, then Eq. (4.7) becomes

$$P_{yy}(\omega) = G_{yx}(\omega)G^{*}_{yx}(\omega) \tag{4.8}$$

Thus the $G_{yx}(\omega)$ functions for the noise simulation of the vertical channel can be derived by applying Eq. (4.8) to each term in Eq. (4.5). The results are as follows.

$$G_{yx}(\omega) = \begin{cases} \dfrac{\sqrt{2\beta_a}}{j\omega+\beta_a}\sigma_a \\ \sqrt{Q_a} \\ \omega^2\dfrac{\sqrt{2\beta_g}}{j\omega+\beta_g}\sigma_g \\ \omega^2\sqrt{Q_g} \end{cases} \tag{4.9}$$

From Eq. (4.4) , the $G_{yx}(\omega)$ functions for the horizontal channels can be obtained as follows:

$$G_{yx}(\omega) = \begin{cases} \dfrac{g}{R}\dfrac{1}{\omega(\omega^2-\omega_s^2)}b_a \\ \dfrac{g}{\omega^2-\omega_s^2} \\ \dfrac{\sqrt{2\beta_a}}{j\omega+\beta_a}\sigma_a \\ \sqrt{Q_a} \\ \omega^2\dfrac{\sqrt{2\beta_g}}{j\omega+\beta_g}\sigma_g \\ \omega^2\sqrt{Q_g} \end{cases} \tag{4.10}$$

Details for the spectrum scaling technique can be found in Smith (1987).

The noise components for the simulated gravity data have been generated one flight at a time. It should be noted that the random noise generator must use a different seed for each flight and for each type of errors. Otherwise, the simulated noise will be correlated. Figure 4.4 shows the noise simulated for case (1). The aircraft velocity is set to be 200 km/h. The coverage of the area is 600 km x 600 km. The intervals for both along and across the flight line are 5 km, which implies 90 sec averaging time.

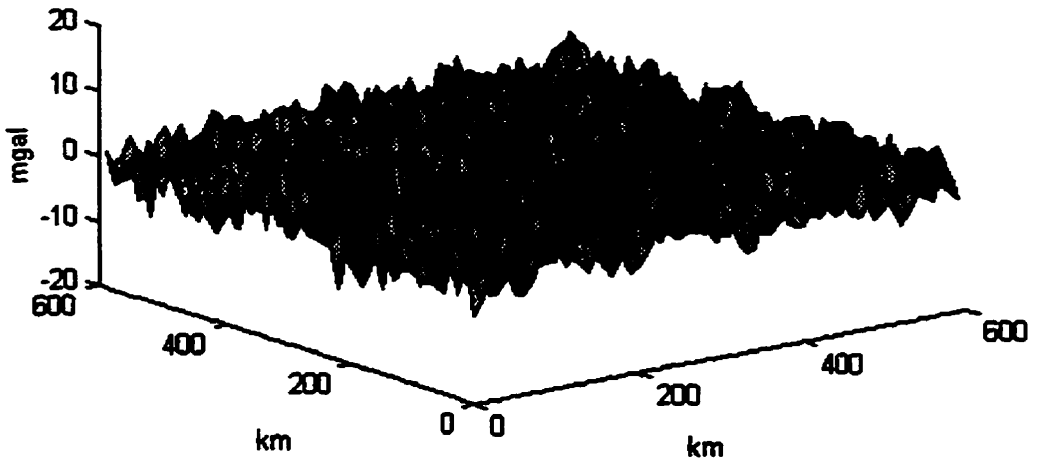

(a) Noise in the vertical channel T_z

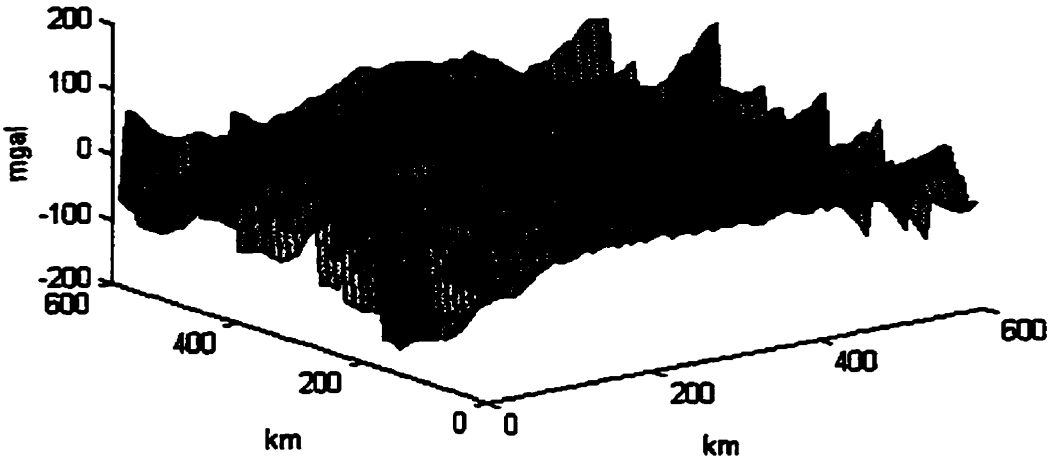

(b) Noise in the horizontal channel T_x

Figure 4.4: Simulated noise before high-pass filtering

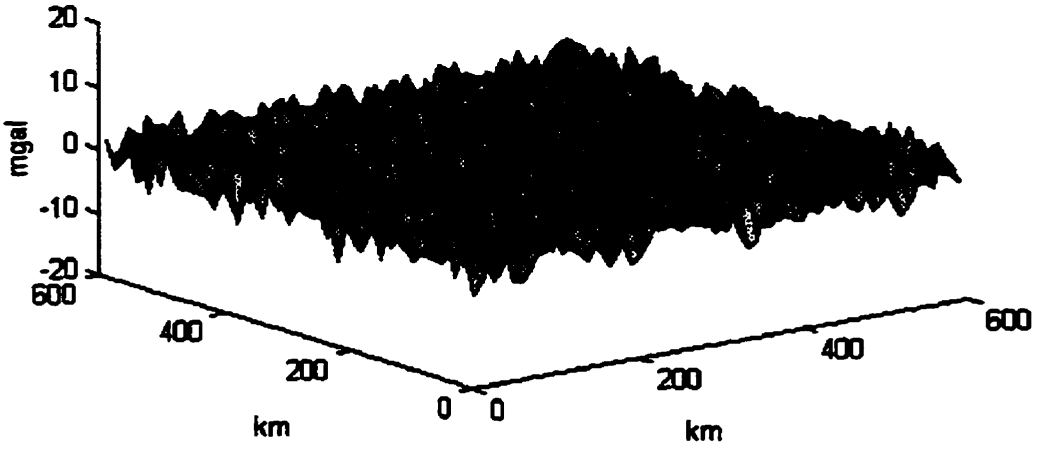

(a) Noise in the vertical channel T_z

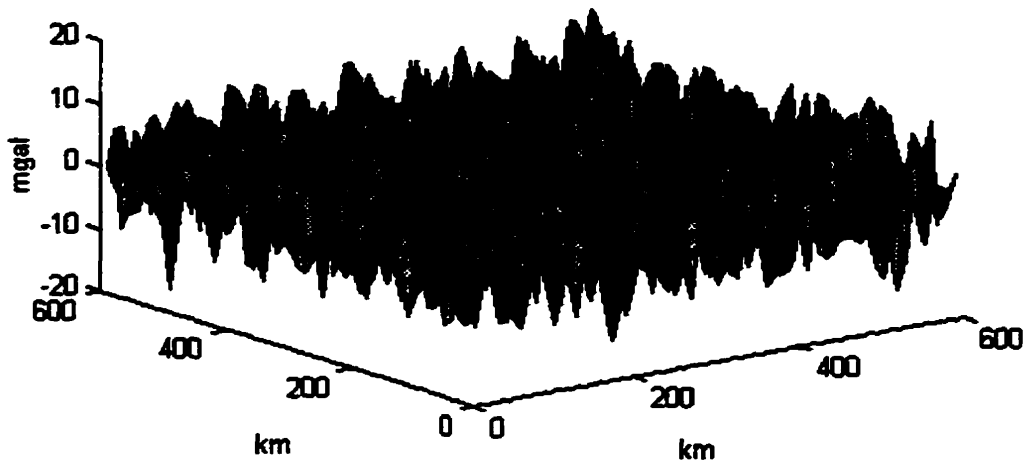

(b) Noise in the horizontal channel T_x

Figure 4.5: Simulated noise after high-pass filtering

As shown in Figure 4.4 (b), low frequency noise dominates the error behaviour in the horizontal channels. The error range in this case is bigger than 350 mgal. This is too big for any type of applications. Fortunately, in each application, the main interest is in signals in a certain band. In geodesy, for instance, the gravity signal in the wavelength range of 10 km to 100 km is of major concern nowadays. The longer wavelength signal has been solved with good accuracy by gravity models. For this reason, numerical test in this thesis will be concentrated on improving the gravity signal in this particular range, i.e. 10 km to 100 km. Thus a high-pass filter is applied to the simulated noise sequences to obtain noises with wavelengths from 10 km to 100 km. The results are illustrated in Figure 4.5. However, it should be pointed out that in areas with sparse terrestrial gravity

observations, longe wavelength signal provided by gravity models are not very reliable. In these areas, gravity signal with wavelength longer than 100 km may need to be determined airborne gravimetry as well.

Assuming that the aircraft velocity is 200 km/h, the 10 km to 100 km wavelength range corresponds to a frequency range of 0.556×10^{-3} to 0.556×10^{-4}. For comparison, the one-dimensional error PSD in this frequency range is shown in Figure 4.6.

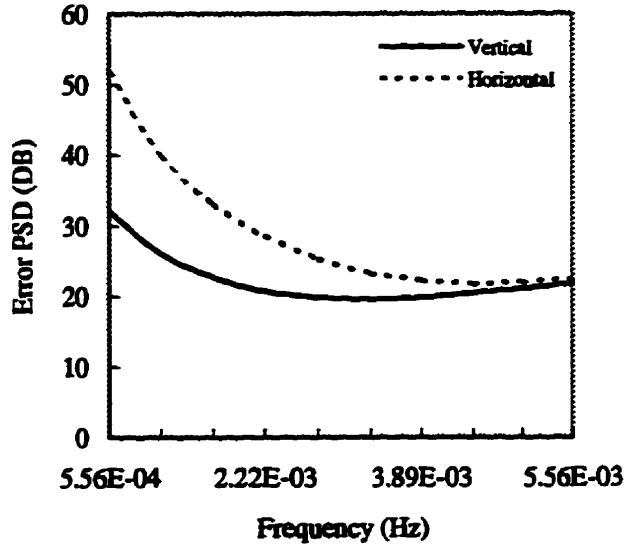

Figure 4.6: 1-D error PSD of airborne vector gravimetry in the interested frequency range

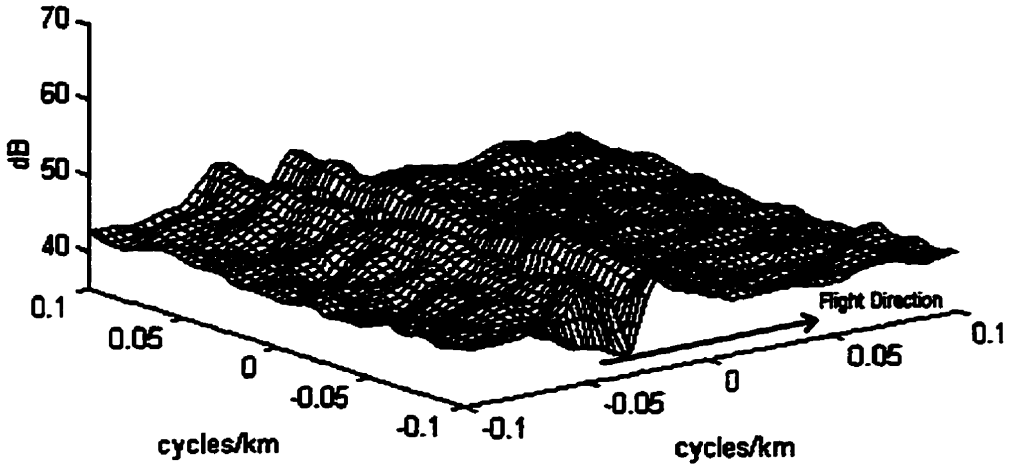

(a) Noise PSD of the vertical component

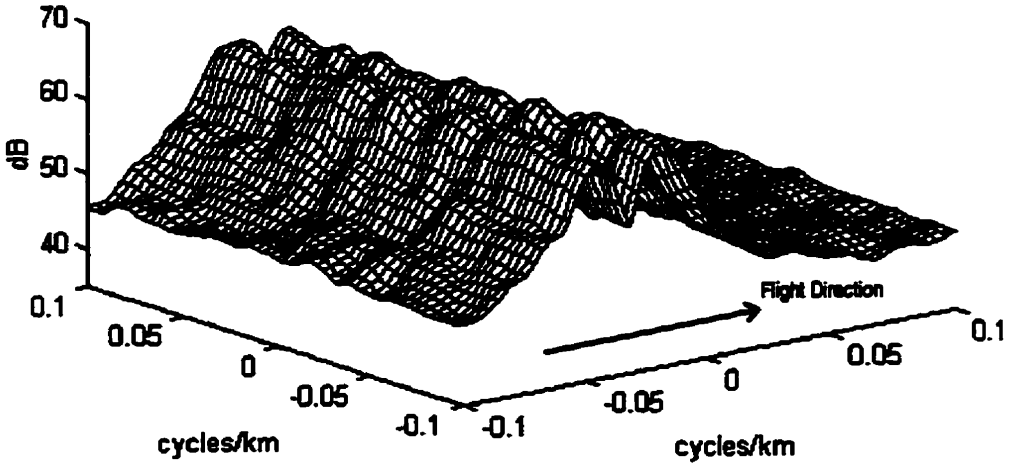

(b) Noise PSD of the horizontal components

Figure 4.7: Noise PSDs of the airborne vector gravimetry for case (1)

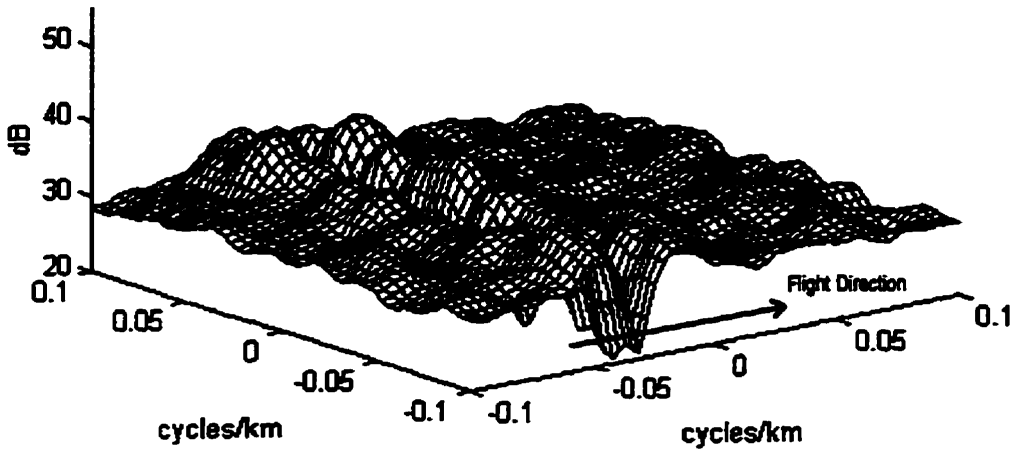

(a) Noise PSD of the vertical component

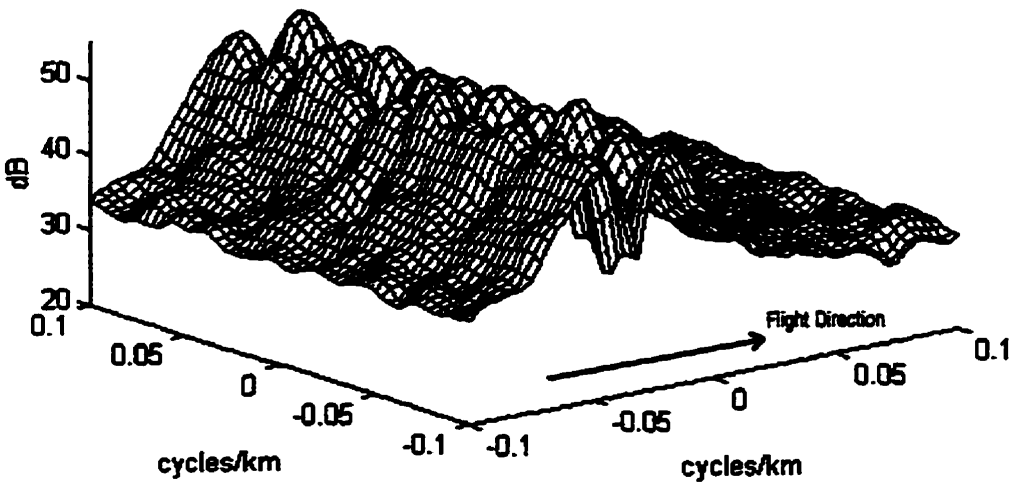

(b) Noise PSD of the horizontal components

Figure 4.8: Noise PSDs of the airborne vector gravimetry for case (2)

After the noise simulations have been done, the PSD estimation method discussed in chapter 2 can be applied. Figure 4.7 shows the results for case (1). Noises for case (2) can be simulated in the same way. The error PSD results for case (2) are shown in Figure 4.8.

In Figure 4.7 and Figure 4.8, it is apparent that the shapes of the 2-D PSDs are mainly due to the flight line direction. In the frequency component corresponding to the along-track direction, the 2-D PSDs behavior very similarly to the 1-D PSD. In the frequency component corresponding to the cross-track direction, the 2-D PSDs have white noise behavior. The expected correlation between the lines (i.e. the none-white noise behavior in the cross track direction) for case (2) has not been shown in Figure 4.8. The reason is that only noise with wavelengths less than 100 km has been simulated, and this makes the correlation between the lines too weak to be detected by the algorithm used here for 2-D PSD estimation.

Obviously, there is another flight route pattern that has to be metioned. That is the cross-over pattern as illustrated in Figure 4.9.

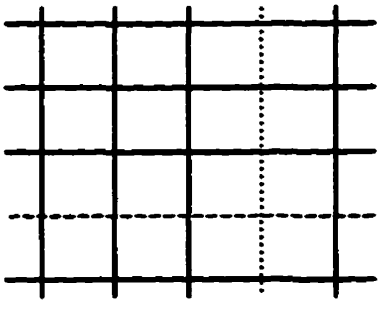

Figure 4.9: Cross-over flight route pattern

Cross-over flight patterns are typically used for controlling constant biases and linear error trends. However, as explained earlier in this section, a band-pass filter would be applied to the airborne gravity measurements for most applications, such as the case in this research. As a result, low frequency signals and noises including constant biases and linear trends will be removed from the raw data. To deal with the cross-over flight pattern problem with the spectral techniques, it is suggested that the cross-over pattern be decomposed into two parallel flight line patterns as shown in Figure 4.10. The two data sets obtained, then, can be easily processed and combined with the multiple-input system techniques discussed in this thesis. If the low frequency contents have not been removed, an additional procedure may be needed to remove or reduce the constant biases and linear trends before the decomposition.

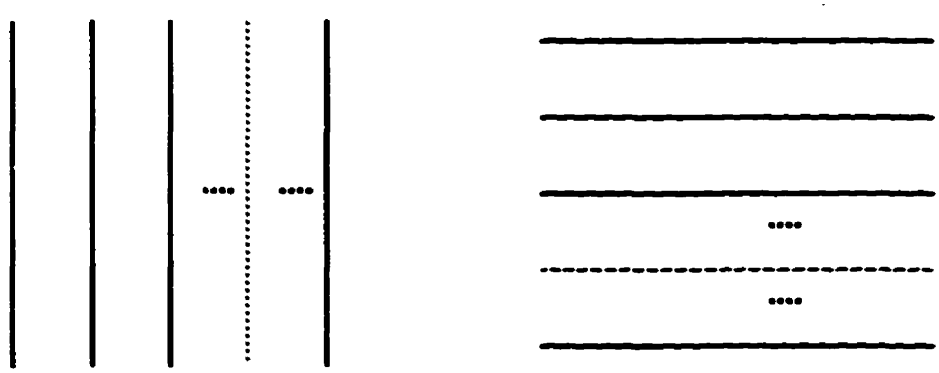

Figure 4.10: The decomposed cross-over flight pattern

The discussion in this section provides a useful 2-D PSD estimation procedure for airborne gravimetry. In reality, the pattern of the flight lines would be neither as shown in case (1) nor as shown in case (2), but the noise sequence for each flight can always be simulated and put together for the 2-D PSD estimation, provided that the one-dimensional PSD models are available.

4.2 STEPWISE IMPLEMENTATION OF A MULTIPLE-INPUT SYSTEM FOR AIRBORNE VECTOR GRAVIMETRY

As mentioned in Section 4 of Chapter 2, the direct determination of the optimum frequency responses of a multiple-input single-output system become very complicated when the number of the input signals is greater than 2. In airborne vector gravimetry, the number of input signals could be three. However, if there are other types of observation to be combined, such as measurements from gradiometry and altimetry, this number would be much larger. In this section, a stepwise procedure is proposed to make the realization easier and to reduce the computer memory requirement. This stepwise procedure repeatedly uses two-input single-output systems. Thus, the two-input system for gravimetry data processing will be discussed first.

If no noise exists, the coherence function between any two of the gravity field quantities (such as the anomalous gravity potential, the components of the gravity disturbance

vector, and the higher order gradients of the anomalous gravity potential) x_1 and x_2 will be equal to one because all of these gravity field quantities are linearly correlated with each other. That is

$$\gamma_{12}^2 = \frac{|P_{12}|^2}{P_{11}P_{22}} = 1 \tag{4.10}$$

where P_{12} is the CPSD of x_1 and x_2, and P_{11} and P_{22} are PSDs of x_1 and x_2, respectively.

The multiple-input theory can not be applied to this case. As a matter of fact, no combination will be required. In practice, however, observations will always be contaminated by noise. Assume that the noise is additive and there is no correlation between signal and noise and no correlation between noise sequences. Then the observations of x_1 and x_2 can be written as $x_{1_o} = x_1 + n_1, x_{2_o} = x_2 + n_2$. Their PSDs and CPSD can be written as

$$\begin{aligned} P_{1_o1_o} &= P_{11} + P_{n_1n_1} \\ P_{2_o2_o} &= P_{22} + P_{n_2n_2} \\ P_{1_o2_o} &= P_{12} \end{aligned} \tag{4.11}$$

The coherence function between the two observations is

$$\gamma_{1_o2_o}^2 = \frac{|P_{1_o2_o}|^2}{P_{1_o1_o}P_{2_o2_o}} = \frac{|P_{12}|^2}{(P_{11} + P_{n_1n_1})(P_{22} + P_{n_2n_2})} \tag{4.12}$$

This coherence function will always be less than 1 and greater than zero. Hence, Eq. (2.35) and Eq. (2.36) can be used here as shown below:

$$H_1 = \frac{P_{1y}}{P_{11}+P_{n_1n_1}} \frac{1-P_{12}\left(P_{22}+P_{n_2n_2}\right)^{-1}P_{2y}P_{1y}^{-1}}{1-\gamma_{1_o2_o}^2}$$

$$H_2 = \frac{P_{2y}}{P_{22}+P_{n_2n_2}} \frac{1-P_{21}\left(P_{11}+P_{n_1n_1}\right)^{-1}P_{1y}P_{2y}^{-1}}{1-\gamma_{1_o2_o}^2} \qquad (4.13)$$

These equations are equivalent to

$$H_1 = \frac{P_{1y}}{P_{11}+P_{n_1n_1}} \frac{1-\dfrac{P_{22}}{P_{22}+P_{n_2n_2}}}{1-\dfrac{P_{11}}{P_{11}+P_{n_1n_1}}\dfrac{P_{22}}{P_{22}+P_{n_2n_2}}}$$

$$H_2 = \frac{P_{2y}}{P_{22}+P_{n_2n_2}} \frac{1-\dfrac{P_{11}}{P_{11}+P_{n_1n_1}}}{1-\dfrac{P_{11}}{P_{11}+P_{n_1n_1}}\dfrac{P_{22}}{P_{22}+P_{n_2n_2}}} \qquad (4.14)$$

When there is no second input signal, i.e. $P_{22}=0$, Eq. (4.14) reduces to Eq. (2.28) which is the optimum frequency response for the single-input system. A more detailed discussion can be found in Sideris (1996).

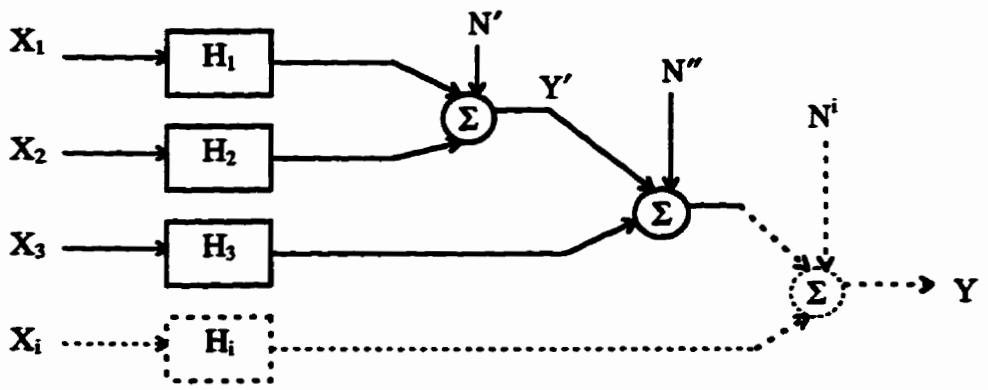

Figure 4.6: A multiple-input system realized by repeatedly using two-input systems

When the number of inputs is more than two, a stepwise procedure for the realization of the system is recommended. First, a two-input system is used to combine two of the input signals. Then, another two-input system is used to combine the output of the first two-input system and the third input signal. After that, if there is a fourth input, a third two-input system can be employed to combine the fourth input with the output of the second two-input system. In this manner, any number of input signals can be combined to obtain one output signal. Thus, a multiple-input single-output system can be implemented by repeatedly using the two-input single-output systems. Essentially, only two-input systems need to be realized. This makes the realization of a multiple-input system much simpler. In addition, the computer memory requirement is greatly reduced because only two inputs will be processed at one time. The implementation procedure proposed is illustrated in Figure 4.6.

Consider a three-input single-output system as an example. For the first two inputs, we have

$$Y' = X_1H_1 + X_2H_2 \tag{4.15}$$

where H_1 and H_2 can be computed with Eq. (4.14). The error PSD of Y' is given by

$$P_{n'n'} = |H_1|^2 P_{n_1n_1} + |H_2|^2 P_{n_2n_2} \tag{4.16}$$

Then the third input and Y' can be combined by another two-input system as follows:

$$Y'' = Y'H_1' + X_3H_2' \tag{4.17}$$

where Y'' is the optimal estimation of the spectrum of the desired output signal Y in this case. H_1' and H_2' is given by

$$H_1' = \frac{P_{yy}}{P_{yy}+P_{n'n'}} \frac{1-\dfrac{P_{33}}{P_{33}+P_{n_3n_3}}}{1-\dfrac{P_{yy}}{P_{yy}+P_{n'n'}}\dfrac{P_{33}}{P_{33}+P_{n_3n_3}}}$$

$$H_2' = \frac{P_{3y}}{P_{33}+P_{n_3n_3}} \frac{1-\dfrac{P_{yy}}{P_{yy}+P_{n'n'}}}{1-\dfrac{P_{yy}}{P_{yy}+P_{n'n'}}\dfrac{P_{33}}{P_{33}+P_{n_3n_3}}} \qquad (4.18)$$

This three-input single-output system will be used in the processing of airborne vector gravity data.

4.3 FREQUENCY DOMAIN LEAST-SQUARES ADJUSTMENT

The concept of the frequency domain least-squares adjustment method can be found in Barzaghi et al. (1993), Sanso and Sona (1995), and Sideris (1996). Unlike the multiple-input system theory, which determines the optimum system frequency response by employing all the PSDs of the input signals and their corresponding error PSDs, the frequency domain least-squares adjustment method assumes that the system frequency response functions are deterministic and are known in advance. In this method, first, the

output spectra corresponding to each of the input signals are computed by multiplying the known frequency response functions with the spectra of the input signals. Then, the optimal estimation of the desired output spectra is obtained according to the least-squares principle. From the remainder of this thesis the frequency domain least-squares adjustment method will be called least-squares adjustment or simply LSA in brief.

Assume that x_{1_o} and x_{2_o} are observations of x_1 and x_2, respectively, that their noises are n_1 and n_2 and are not correlated, and that the signal to be estimated is y. In the frequency domain, the spectra of y corresponding to each of the observations can be written as

$$\begin{aligned} Y^1 &= H_1 X_{1_o} \\ Y^2 &= H_2 X_{2_o} \end{aligned} \tag{4.19}$$

where the frequency response functions H_1 and H_2 are considered perfectly known. The PSDs of the errors in Y^1 and Y^2 are given by

$$\begin{aligned} P^1_{n_y n_y} &= H_1^2 P_{n_1 n_1} \\ P^2_{n_y n_y} &= H_2^2 P_{n_2 n_2} \end{aligned} \tag{4.20}$$

Transfering least-squares principle to the spectral domain, the optimal estimation of Y is defined as the weighted average of Y^1 and Y^2. The weight assigned for each spectra is the inverse of its error PSD. Thus

$$\hat{Y} = \frac{\frac{1}{P^1_{n_y n_y}}}{\frac{1}{P^1_{n_y n_y}} + \frac{1}{P^2_{n_y n_y}}} Y^1 + \frac{\frac{1}{P^2_{n_y n_y}}}{\frac{1}{P^1_{n_y n_y}} + \frac{1}{P^2_{n_y n_y}}} Y^2 \tag{4.21}$$

By substituting Eq. (4.20) into Eq. (4.21), we get

$$\hat{Y} = \left(1 + \frac{H_1^2 P_{n_1 n_1}}{H_2^2 P_{n_2 n_2}}\right)^{-1} H_1 X_{1_o} + \left(1 + \frac{H_2^2 P_{n_2 n_2}}{H_1^2 P_{n_1 n_1}}\right)^{-1} H_2 X_{2_o} \tag{4.22}$$

The error PSD of $\hat{Y}$ is expressed by

$$P_{nn} = \left(H_1^{-2} P_{n_1 n_1}^{-1} + H_2^{-2} P_{n_2 n_2}^{-1}\right)^{-1} \tag{4.23}$$

Similarly, when there are three or more observations, the optimal estimation of y and its error PSD expression can be obtained as follows:

$$\begin{aligned} \hat{Y} = & \left(1 + \frac{H_1^2 P_{n_1 n_1}}{H_2^2 P_{n_2 n_2}} + \frac{H_1^2 P_{n_1 n_1}}{H_3^2 P_{n_3 n_3}}\right)^{-1} H_1 X_{1_o} + \left(1 + \frac{H_2^2 P_{n_2 n_2}}{H_1^2 P_{n_1 n_1}} + \frac{H_2^2 P_{n_2 n_2}}{H_3^2 P_{n_3 n_3}}\right)^{-1} H_2 X_{2_o} \\ & + \left(1 + \frac{H_3^2 P_{n_3 n_3}}{H_1^2 P_{n_1 n_1}} + \frac{H_3^2 P_{n_3 n_3}}{H_2^2 P_{n_2 n_2}}\right)^{-1} H_3 X_{3_o} \end{aligned} \tag{4.24}$$

$$P_{nn} = \left(H_1^{-2} P_{n_1 n_1}^{-1} + H_2^{-2} P_{n_2 n_2}^{-1} + H_3^{-2} P_{n_3 n_3}^{-1}\right)^{-1} \tag{4.25}$$

Eq. (4.24) and Eq. (4.25) can be easily expanded for the general case, for example, when k observations exist:

$$\begin{aligned} \hat{Y} = & \left(1 + \frac{H_1^2 P_{n_1 n_1}}{H_2^2 P_{n_2 n_2}} + \frac{H_1^2 P_{n_1 n_1}}{H_3^2 P_{n_3 n_3}} + \cdots + \frac{H_1^2 P_{n_1 n_1}}{H_k^2 P_{n_k n_k}}\right)^{-1} H_1 X_{1_o} \\ & + \left(\frac{H_2^2 P_{n_2 n_2}}{H_1^2 P_{n_1 n_1}} + 1 + \frac{H_2^2 P_{n_2 n_2}}{H_3^2 P_{n_3 n_3}} + \cdots + \frac{H_2^2 P_{n_2 n_2}}{H_k^2 P_{n_k n_k}}\right)^{-1} H_2 X_{2_o} \\ & + \cdots + \left(\frac{H_k^2 P_{n_k n_k}}{H_1^2 P_{n_1 n_1}} + \frac{H_k^2 P_{n_k n_k}}{H_2^2 P_{n_2 n_2}} + \cdots + \frac{H_k^2 P_{n_k n_k}}{H_{k-1}^2 P_{n_{k-1} n_{k-1}}} + 1\right)^{-1} H_k X_{k_o} \end{aligned} \tag{4.26}$$

$$P_{nn} = \left(H_1^{-2}P_{n_1n_1}^{-1} + H_2^{-2}P_{n_2n_2}^{-1} + H_3^{-2}P_{n_3n_3}^{-1} + \cdots + H_k^{-2}P_{n_kn_k}^{-1}\right)^{-1} \tag{4.27}$$

The known frequency response functions, i.e. H_1, H_2,..., are chosen as the frequency responses of the ideal single-input single-output system. These ideal frequency responses for airborne vector gravimetry can be obtained by using the PSD and CPSD relations given in Section 3.2. For example, assume that the input signals are T_x, T_y, and T_z, i.e. all the components of the gravity disturbance vector. The output signal is the vertical component T_z, and the ideal frequency responses will be

$$H_1 = \frac{P_{T_zT_z}}{P_{T_xT_x}} = \frac{-j4\pi^2 uqP_{TT}}{4\pi^2 u^2 P_{TT}} = -j\frac{q}{u} \tag{4.28}$$

$$H_2 = \frac{P_{T_yT_z}}{P_{T_yT_y}} = \frac{-j4\pi^2 vqP_{TT}}{4\pi^2 v^2 P_{TT}} = -j\frac{q}{v} \tag{4.29}$$

$$H_3 = \frac{P_{T_zT_z}}{P_{T_zT_z}} = 1 \tag{4.30}$$

From Eq. (4.28) to Eq. (4.30), it can be seen that no prior information about the gravity field is needed if the ideal frequency response functions of the single-input single-output systems are used as the known frequency response functions in the least-squares adjustment method. All the ideal frequency response functions used in this research for the data processing in airborne vector gravimetry are listed in Table 4.2.

Table 4.2: List of Ideal Frequency Responses Used for The Airborne Vector Gravimetry Data Processing

Output Signal	Input Signal	Frequency Response
T_z	T_x	-jq/u
	T_y	-jq/v
	T_z	1
T_x	T_x	1
	T_y	u/v
	T_z	-ju/q
T_y	T_x	v/u
	T_y	1
	T_z	-jv/q
T	T_x	-j/(2πu)
	T_y	-j/(2πv)
	T_z	-1/(2πq)

4.4 SOME PRACTICAL CONSIDERATIONS

4.4.1 Combining observations at different levels

The multiple-input single-output system and the least-squares adjustment method can be modified to combine observations made on different level surfaces and to give results at any altitude. This means that the methods will possess built-in functions to deal with the downward and upward continuation problems.

In Section 3.3, the analytical kernels for upward and downward continuation in the frequency domain have been discussed. For upward continuation, we have

$$K_u = e^{-2\pi H\sqrt{u^2+v^2}} \tag{4.31}$$

For downward continuation, we have

$$K_d = e^{2\pi H\sqrt{u^2+v^2}} \tag{4.32}$$

where, in Eq. (4.31) and Eq. (4.32), H is the elevation difference between the two level surfaces. Notice that the only difference between these two kernels is the sign of the exponent. This sign difference can be taken care of by using the height (the z coordinate) difference between the two level surfaces instead of the absolute distance. Assuming that the height of the measurement surface is h_1 and the height of the destination surface is h_2, we obtain

$$K = e^{2\pi(h_1-h_2)\sqrt{u^2+v^2}} \tag{4.33}$$

Obviously, in the case of upward continuation ($h_2 > h_1$), K will be equal to K_u. In contrast, in the case of downward continuation ($h_2 < h_1$), K will equal K_d. Hence, K can be called the continuation kernel.

To build the continuation ability into a multiple-input system or a least-squares adjustment solution, we need to consider not only the continuation of the input signals but the continuation of the input noise PSDs as well. These two types of continuation can be done very easily in the frequency domain. Multiplying an input signal by its corresponding continuation kernel, we get the signal at the destination altitude. To obtain the continuation of an input noise PSD, we only need to multiply it by the square of the corresponding continuation kernel. The expressions are as follows:

$$X_i^c = X_i K_i \tag{4.34}$$

$$P_{n_i n_i}^c = P_{n_i n_i} K_i^2 \tag{4.35}$$

where X_i^c is the continuation of the input signal X_i, $P_{n_i n_i}^c$ is the continuation of the the input noise PSD $P_{n_i n_i}$, and K_i is computed by Eq. (4.33) according to the height of X_i and the height of X_i^c. In case that K_i is used as a kernel for downward continuation, the instability discussed in Section 3.3.1 should be noticed. With Eq. (4.33) to Eq. (4.35), we can readily build the continuation ability into a multiple-input system or a least-squares adjustment solution so that it will be able to combine observations at different levels.

4.4.2 Accuracy Improvement Without Noise PSD Information

To improve the accuracy in airborne vector gravimetry without noise PSD information, we have to exploit the following two facts :

1. The vertical component is much more accurate than the horizontal components.
2. The PSDs of the horizontal gravity components can be determined from the PSD of the vertical component.

Thus, if $\bar{P}_{T_zT_z}$ is the PSD of the measurements of the vertical component, we have

$$\begin{aligned} P_{T_xT_x} &= \frac{u^2}{q^2}\bar{P}_{T_zT_z} \\ P_{T_yT_y} &= \frac{v^2}{q^2}\bar{P}_{T_zT_z} \end{aligned} \tag{4.36}$$

$P_{T_xT_x}$ and $P_{T_yT_y}$ are not the PSDs of the true signals of the horizontal components because $\bar{P}_{T_zT_z}$ is contaminated by the measurement noise. However, because the noise level is much lower in the vertical channel and u and v in Eq. (4.36) are generally less than q (so that the power of the noise will be attenuated), $P_{T_xT_x}$ and $P_{T_yT_y}$ can be treated as reasonable estimates of the true PSDs of the horizontal components in this case. Therefore, we can improve the horizontal components with the Wiener filter:

$$\begin{aligned} \hat{T}_x &= F^{-1}\left\{\frac{P_{T_xT_x}}{\bar{P}_{T_zT_z}}F\{T_{x_o}\}\right\} = F^{-1}\left\{\frac{u^2}{q^2}\frac{\bar{P}_{T_zT_z}}{\bar{P}_{T_zT_z}}F\{T_{x_o}\}\right\} \\ \hat{T}_y &= F^{-1}\left\{\frac{P_{T_yT_y}}{\bar{P}_{T_yT_y}}F\{T_{y_o}\}\right\} = F^{-1}\left\{\frac{v^2}{q^2}\frac{\bar{P}_{T_zT_z}}{\bar{P}_{T_zT_z}}F\{T_{y_o}\}\right\} \end{aligned} \tag{4.37}$$

where $\overline{P}_{T_xT_x}$ and $\overline{P}_{T_yT_y}$ are the PSDs of the observations of the two horizontal components. Further improvements for all three components can be achieved with the least-squares adjustment method if their noises are not correlated with each other. The reason is that only the magnitude spectra are used in the Wiener filters and so the noise could be reduced by averaging due to their random phases. Because detailed information on the noise PSDs is not available, we have assumed that the accuracies of all three components are the same after the application of the Wiener filter in Eq. (4.37). Eq. (4.26) then becomes

$$\begin{aligned}\hat{Y} = &\left(1+\frac{H_1^2}{H_2^2}+\frac{H_1^2}{H_3^2}+\cdots+\frac{H_1^2}{H_k^2}\right)^{-1} H_1 X_{1_o} \\ &+\left(\frac{H_2^2}{H_1^2}+1+\frac{H_2^2}{H_3^2}+\cdots+\frac{H_2^2}{H_k^2}\right)^{-1} H_2 X_{2_o} \\ &+\cdots+\left(\frac{H_k^2}{H_1^2}+\frac{H_k^2}{H_2^2}+\cdots+\frac{H_k^2}{H_{k-1}^2}+1\right)^{-1} H_k X_{k_o}\end{aligned} \tag{4.38}$$

where X_{i_o} , i=1,2,3...k could be the spectra of the vertical component observation or the spectra of any of the horizontal components obtained with Eq. (4.37), and $\hat{Y}$ could be the improved spectra of any component of the gravity disturbance vector.

CHAPTER 5

NUMERICAL TESTS AND ANALYSIS

In this chapter, after an introduction to the data simulation, results of the numerical tests are shown and analyzed. The tests are focused on getting accurate results from airborne observations using spectral methods with or without measurement noise PSD information. The tests also investigate some aspects of downward continuation of airborne gravimetry data to a level surface and to the surface of the Earth. Some comparison between different processing methods is also done. Finally, the accuracy of geoid determination using airborne gravity data is investigated.

5.1 DATA SIMULATION

Airborne vector gravimetry measurements are simulated in this section. First a local gravity field is modeled with a two-layer point mass model. Then the noise for each channel of airborne vector gravimetry is simulated and added to the corresponding component of the simulated gravity disturbance vector.

The point mass model has been widely used in local anomalous gravity field modeling (Forsberg, 1984; Vassiliou, 1985 and 1986). The basic idea of this model is that the anomalous gravity field can be generated (or modeled) by one or several anomalous point mass layers under and parallel to the Earth's surface. In practice, most of the time, these anomalous point mass layers are computed from the existing gravity anomalies or disturbances by using a deconvolution procedure. If the known gravity disturbances are gridded, spectral techniques can be used to greatly alleviate the computation load. The mathematical models needed for the gravity field simulation using the point mass model are given directly here in the space domain and in the frequency domain. Details can be found in Forsberg (1984) and Vassiliou (1986).

The same local coordinate system introduced in Chapter 3 is used in the following description. Assuming the anomalous masses on one layer at depth d, the gravity disturbance at a point P (x_p, y_p, z_p) can be expressed as

$$\delta g(x_p, y_p, z_p) = G \sum_{i=1}^{M} \sum_{j=1}^{N} \frac{d + z_p}{\left[(x_i - x_p)^2 + (y_j - y_p)^2 + (d + z_p)^2 \right]^{3/2}} \rho(x_i, y_j) \qquad (5.1)$$

where G is the Newton's gravitational constant, x_i, y_j are the coordinates of the point mass $\rho(x_i, y_j)$ and M, N are the number of points in the x and y directions respectively. The right-hand side of this equation is a two-dimensional convolution. With the use of the two-dimensional discrete Fourier transform, all

gravity disturbances in the corresponding grid at an altitude z_0 can be computed at the same time. Eq. (5.1) in the frequency domain becomes

$$\delta g(x,y,z_0) = G\,F^{-1}\left\{F\left\{\frac{d+z_0}{\left[x^2+y^2+(d+z_0)^2\right]^{3/2}}\right\}F\{\rho(x,y)\}\right\} \tag{5.2}$$

As mentioned in Chapter 3, the Fourier transform of the kernel function has an analytical expression. Eq. (5.2) can thus be rewritten as

$$\delta g(x,y,z_0) = G\,F^{-1}\left\{2\pi e^{-2\pi q(d+z_0)}F\{\rho(x,y)\}\right\} \tag{5.3}$$

To obtain the anomalous point masses from the existing gravity disturbance data, we invert Eq. (5.3) as

$$\rho(x,y) = \frac{1}{2\pi G}\,F^{-1}\left\{e^{2\pi q(d+z_0)}F\{\delta g(x,y,z_0)\}\right\} \tag{5.4}$$

The expressions for the two horizontal components generated by the anomalous masses of a single layer are given by

$$T_x(x_p,y_p,z_p) = G\sum_{i=1}^{M}\sum_{j=1}^{N}\frac{x_i-x_p}{\left[(x_i-x_p)^2+(y_j-y_p)^2+(d+z_p)^2\right]^{3/2}}\,\rho(x_i,y_j) \tag{5.5}$$

$$T_x(x,y,z_0) = G\,F^{-1}\left\{j\frac{2\pi u}{q}e^{-2\pi q(d+z_0)}F\{\rho(x,y)\}\right\} \tag{5.6}$$

$$T_y(x_p,y_p,z_p) = G\sum_{i=1}^{M}\sum_{j=1}^{N}\frac{y_i-y_p}{\left[(x_i-x_p)^2+(y_j-y_p)^2+(d+z_p)^2\right]^{3/2}}\,\rho(x_i,y_j) \tag{5.7}$$

$$T_y(x,y,z_0) = G\,F^{-1}\left\{ j\frac{2\pi v}{q} e^{-2\pi q(d+z_0)} F\{\rho(x,y)\} \right\} \qquad (5.8)$$

The local gravity field used in this research is simulated on a 5 km x 5 km grid. The total coverage is 600 x 600 km^2. Generally, a low frequency signal will be more accurately simulated by a deep point mass layer and high frequency signal will be more accurately simulated by a shallow point mass layer. To be more realistic, a multi-layer model should be used to account for signals in different frequency ranges (Forsberg, 1984). A two-layer model is used to simulate the gravity signals in the wavelength range of 10 km to 100 km which is the wavelength range selected for this research. Thus, the actual simulation procedure starts with high pass filtering the known gravity disturbance data to filter out the signals with wavelengths longer than 100 km, which is equivalent to removing the low frequency signal by subtracting an errorless global gravity field model. Then the residual is further split into two data sets. One contains signals with wavelengths shorter than 30 km. The other contains signals in the wavelength range of 30 km to 100 km. After that, a point mass layer buried 10 km below the geoid is generated using the first data set with Eq. (5.4). And another point mass layer buried 30 km below the geoid is generated using the the second second data set. Finally, the gravity field components at any altitude can be computed with the formulae given. A check of results shows no discrepancies between the input known gravity disturbances and those simulated. This, however, does not mean that the actual gravity field has been reproduced by the

two-layer model, especially at other height levels. What can be expected is that the simulated gravity field would be close to the actual gravity field. By using the generated point masses to compute all the three components of the gravity disturbance vector at different levels, a consistent gravity field can be obtained to work with. Table 5.1 lists the statistics of the components of the simulated gravity disturbance vector on the zero height level surface. The graphic presentations of these components are shown in Figures 5.1, 5.2, and 5.3, respectively. The signal PSD estimates are illustrated in Figure 5.4.

Noise in airborne vector gravimetry data is simulated with the spectrum scaling technique which has been discussed in Section 4.1. The whole area is assumed to have been surveyed by a number of parallel flights, following case (1) discussed in Section 4.1. The simulated noise for the vertical channel and the two horizontal channels are shown in Figures 5.5, 5.6, 5.7. Their statistics are given in Table 5.2. The noise PSDs are shown in Figure 4.7 in Section 4.1.2.

Table 5.1: Statistics of the Simulated Gravity Vector Components

Gravity Vector Component	Min	Max	Mean	RMS
T_z (mgal)	-54.2	88.0	0.00	11.98
T_x (mgal)	-53.4	39.0	0.00	7.70
T_y (mgal)	-75.0	52.3	0.00	9.11

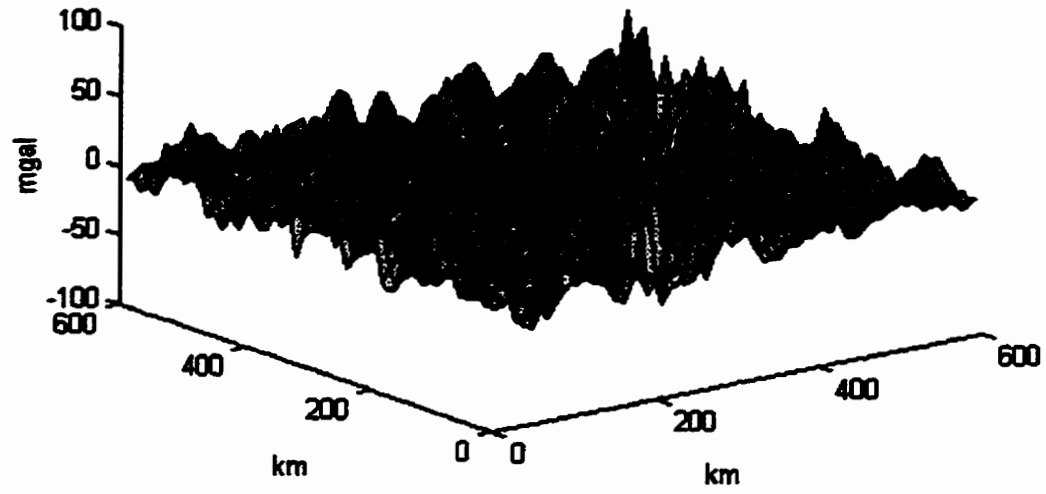

Figure 5.1: Graphic presentation of simulated T_z

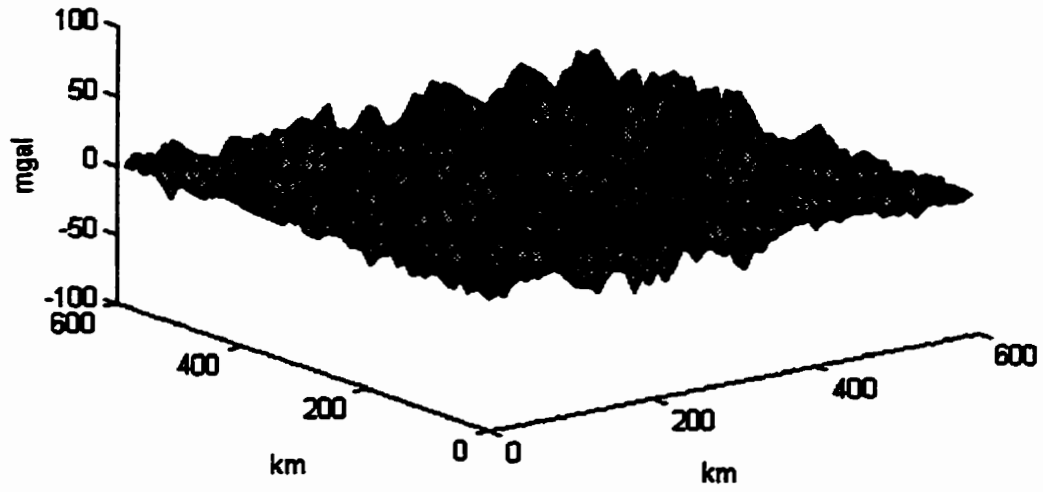

Figure 5.2: Graphic presentation of simulated T_x

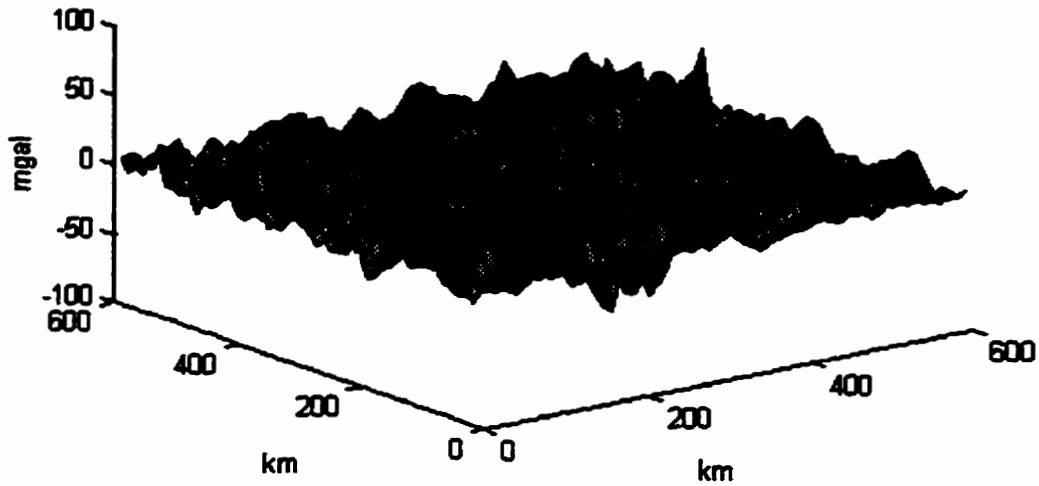

Figure 5.3: Graphic presentation of simulated T_y

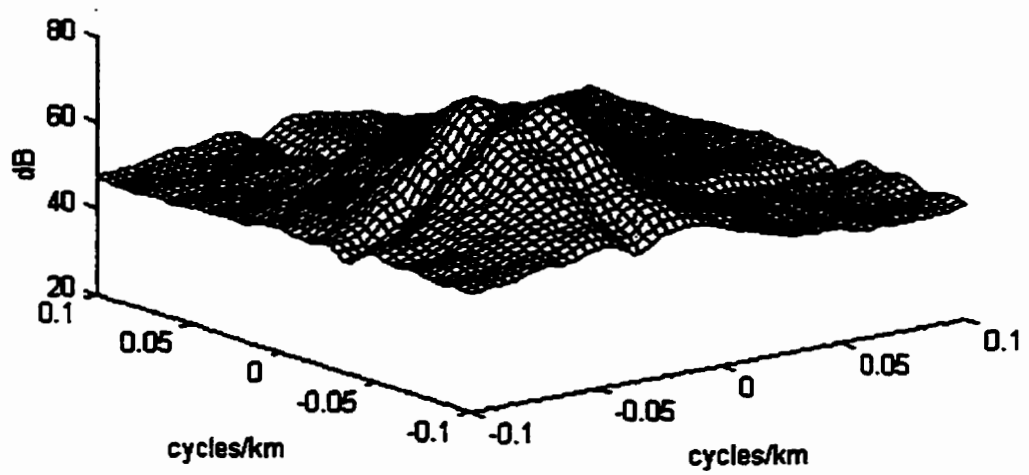

(a) Signal PSD of T_z

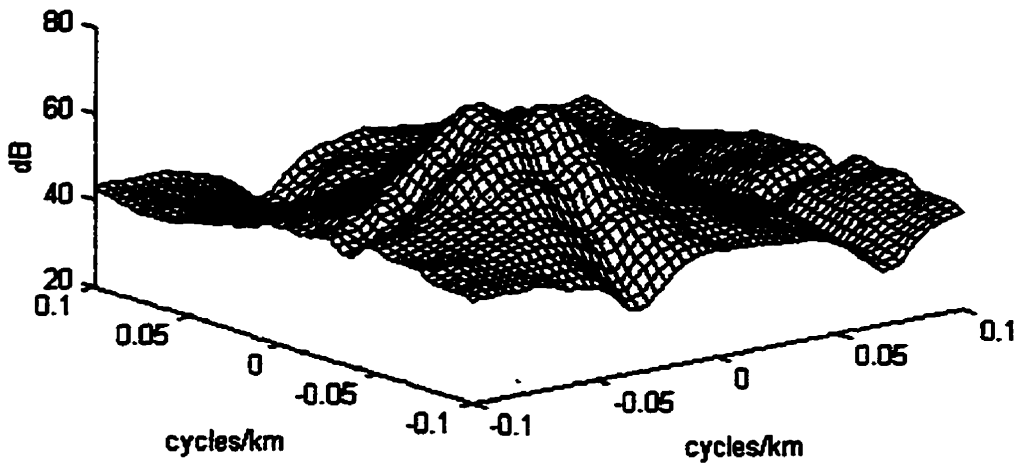

(b) Signal PSD of T_x

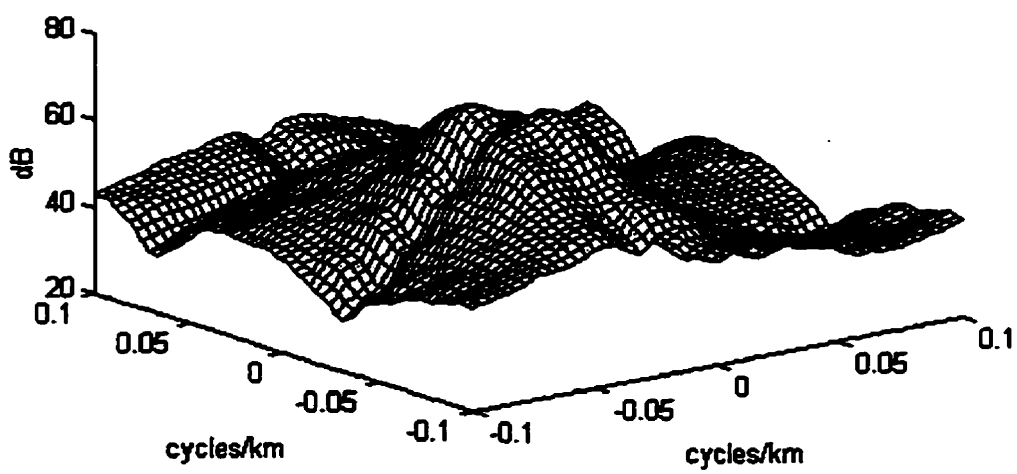

(c) Signal PSD of T_y

Figure 5.4: Signal PSDs of simulated gravity disturbance vector components

Table 5.2: Statistics of the Simulated Airborne Vector Gravimetry Noise

Channel	Min	Max	Mean	Std. Dev.
T_z (mgal)	-8.6	5.5	0.19	2.16
T_x (mgal)	-19.4	14.8	0.13	4.96
T_y (mgal)	-18.0	18.5	-0.10	4.81

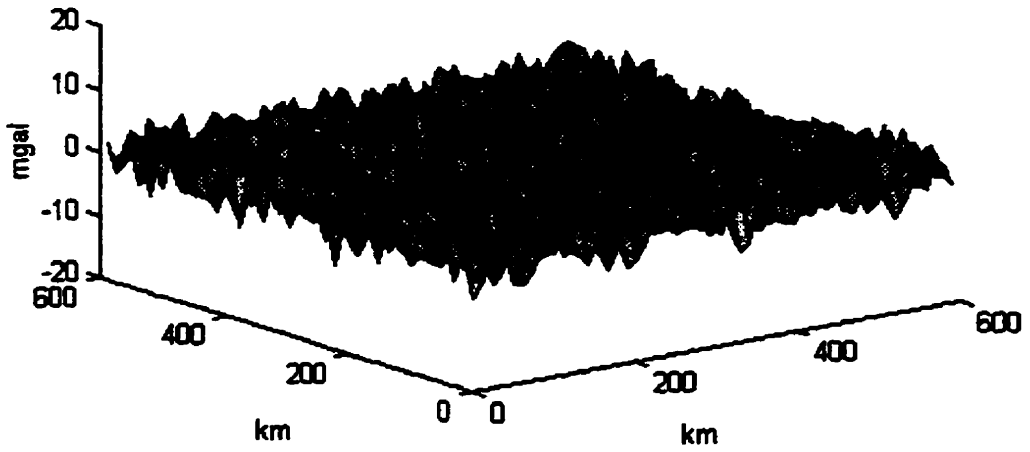

Figure 5.5: Graphic presentation of the simulated noise for T_z

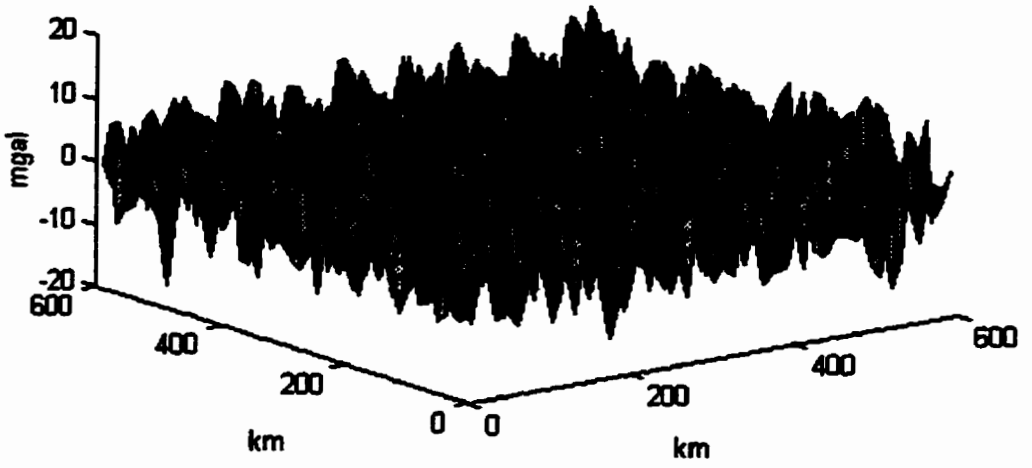

Figure 5.6: Graphic presentation of the simulated noise for T_x

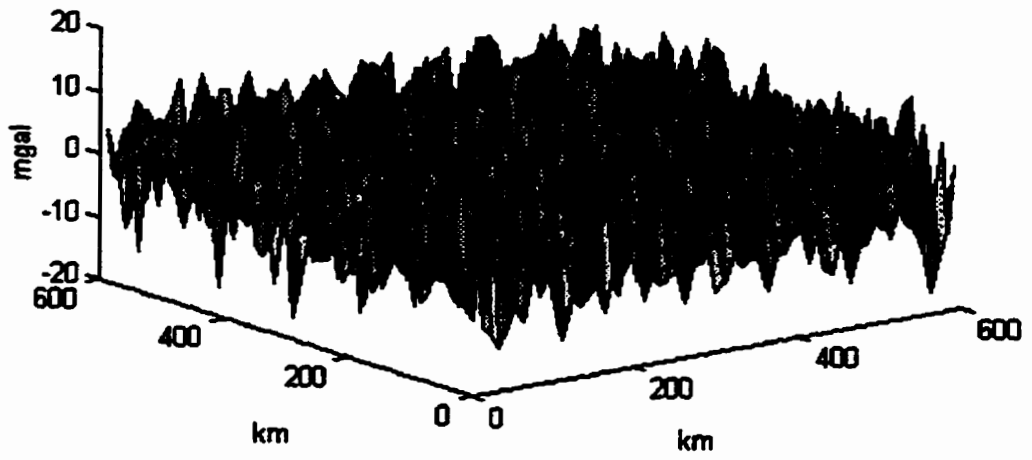

Figure 5.7: Graphic presentation of the simulated noise for T_y

5.2 ACCURACY IMPROVEMENT WITH NOISE PSD INFORMATION

The effectiveness of spectral methods in improving the accuracy of the airborne gravity disturbance vector is tested in this and the following sections. In this section, we assume that the noise PSDs for all the channels of airborne vector gravimetry are available. Zero padding is used in all numerical computations in this thesis to acount for the circular convolution effect. To avoid edge effects due to the limited coverage, in this section as well as in following sections, all the comparisons of the estimated signals and the true signals are done in an inner area that is 50 km inside the borders of the total area.

Usually, only the one-dimensional noise PSDs are available. Before the multiple-input single-output system can be implemented, all the required two-dimensional noise PSDs must be estimated. Generally, there is no analytical way to derive the two-dimensional PSD model from the one-dimensional PSD model. Instead, the numerical estimation method proposed in Section 4.1 will be used.

Using the stepwise procedure, software has been written in which the realized multiple-input system can take as many as ten types of gravity field quantities (including the anomalous potential and all of its first and second order gradients) as its inputs and give any one of these quantities as its output. In the case of airborne vector gravimetry, the maximum number of input signals is three. When

there is only one input signal, the single-input single-output system gives the same results as the two-dimensional Wiener filter.

Table 5.3: Accuracy Comparison of Different Combinations With Multiple-Input Single-Output System

Output Signal	Input Signals	Min	Max	Mean	Std. Dev.
T_z (mgal)	T_z	-4.5	4.8	0.01	1.28
	T_z T_x	-4.6	4.4	-0.00	1.18
	T_z T_y	-4.8	5.3	0.01	1.20
	T_z T_x T_y	-4.5	4.5	0.01	1.14
T_x (mgal)	T_x	-6.5	6.9	0.00	1.81
	T_x T_z	-3.0	2.8	0.00	0.73
	T_x T_y	-5.6	5.1	0.00	1.41
	T_x T_z T_y	-2.7	3.0	0.00	0.72
T_y (mgal)	T_y	-7.9	6.7	0.00	2.02
	T_y T_z	-3.2	3.3	0.00	0.83
	T_y T_x	-6.8	5.6	0.01	1.63
	T_y T_z T_x	-3.2	3.0	0.00	0.81

Table 5.3 shows the accuracies of the results for different input combinations for each component of the gravity disturbance vector. All the estimations are done at flight level, i.e., no downward continuation is made. A significant improvement for every component is seen after the Wiener filtering. Adding other components, additional improvements for the vertical component T_z and the two horizontal components T_x, T_y are different. The further improvement for T_z is much less than those for T_x and T_y. Moreover, the best results for T_x and T_y have significantly higher accuracy than the best result for T_z. The reason for that can easily be illustrated in the frequency domain. Most of the time, u and v are less than $q=(u^2 + v^2)^{1/2}$. When T_x and/or T_y are used to improve the results of T_z, the noise in T_x and T_y will be amplified by a factor of q/u or q/v in each frequency. In this case, the system will be more dependent on the measurements of T_z. Thus, less improvement will be seen. In contrast, when T_z is used to improve the two horizontal components, the noise in T_z will be attenuated by a factor of u/q or v/q. This means that T_x or T_y will get a set of much more accurate measurements. The measurements will be even more accurate than the original measurements of T_z. This explains why the final results for T_x and T_y are better than the results for T_z.

To give a perspective view of how the multiple-input system works to improve the results, surface maps of the errors are plotted in the total area. Figure 5.8 shows the error in T_z after Wiener filtering (i.e., when the input is only T_z). Figure 5.9 displays the error in T_z estimated by combining T_z with T_x and T_y. Errors in the

estimations of T_x are presented to show the improvement in the horizontal components. Shown in Figure 5.10 are the errors in T_x after Wiener filtering. Errors in T_x estimated from T_x, T_z and T_y together are shown in Figure 5.11.

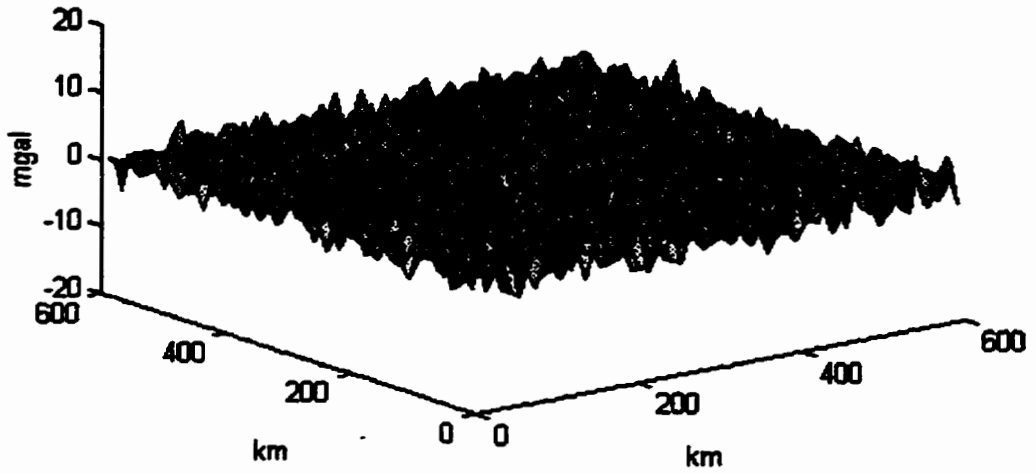

Figure 5.8: Error in T_z after Wiener filtering

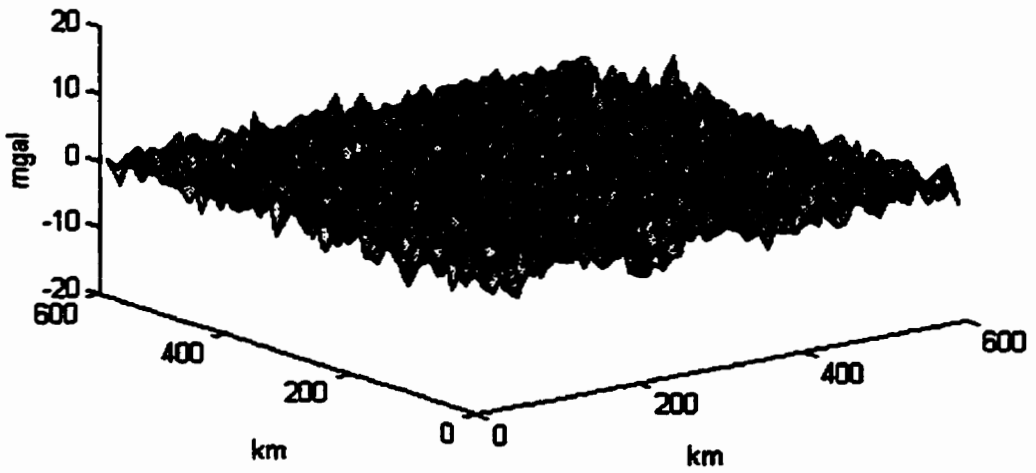

Figure 5.9: Error in T_z estimated by combining T_z with T_x, T_y

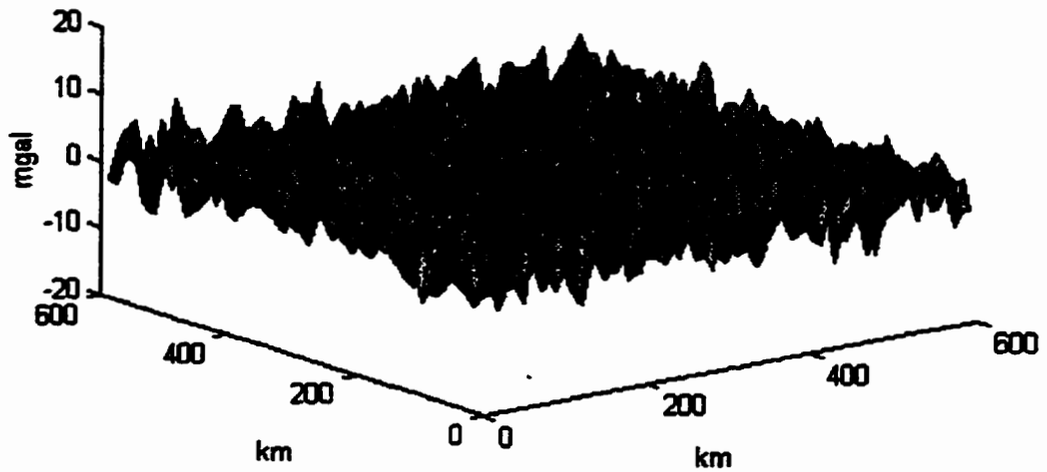

Figure 5.10: Error in T_x after Wiener filtering

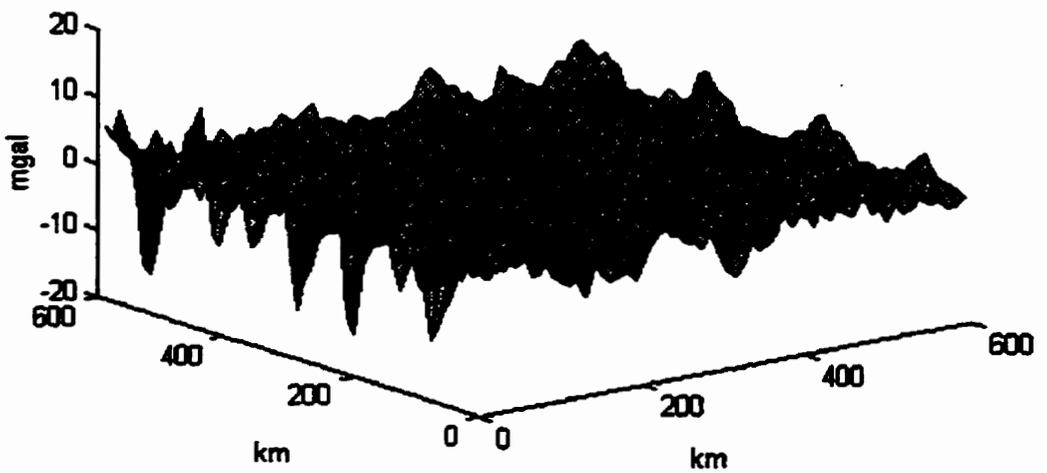

Figure 5.11: Error in T_x estimated by combining T_x with T_z, T_y

Comparing Figure 5.8 with Figure 5.5 and Figure 5.10 with Figure 5.6, we can see improvement in both the border and inner areas. By comparing Figures 5.8, 5.9 and Figures 5.10, 5.11 to examine the effect of other inputs, it is seen that higher accuracies are obtained in the inner area while accuracies are lower toward the borders. The reason for this trend is that, in the single input case, no prediction for one signal from other types of signals is used, while in the multiple input case, such a prediction is necessary. These predictions, which are well-known in physical geodesy, require a large area of coverage depending on the wavelength range of the signal to be recovered. Thus, it is the prediction between signals that causes the accuracy degradation in the border area. This is the price to be paid when higher accuracy is desired in the inner area. As expected, it is also seen that the high frequency noise is reduced by the input signal combination.

Obviously, another approach can be used in the case that the one-dimensional noise PSDs are known. First, a one-dimensional Wiener filter can be applied to each flight trajectory. Then, the combinations can be made by employing the least-squares adjustment method in the two-dimensional frequency domain. To evaluate this approach, the first step is to compare the results from the one-dimensional Wiener filter with the results from the single-input single-output system system (i.e. the two-dimensional Wiener filter). Table 5.4 indicates the accuracies of the results using one-dimensional Wiener filters.

Table 5.4: Accuracies of Gravity Vector Components After Wiener Filtering Along Trajectories

Gravity Vector Components	Min	Max	Mean	Std. Dev.
T_z (mgal)	-6.0	6.7	0.02	1.83
T_x (mgal)	-9.7	9.8	-0.05	2.34
T_y (mgal)	-12.4	11.0	0.01	3.00

Comparing the numbers in Table 5.4 with their corresponding results from the input-output system in Table 5.3, we can see that the one-dimensional Wiener filtering gives less accurate results although some improvements can be expected. The possible reason is that fewer measurements are used in one-dimensional Wiener filtering. Because the two-dimensional filtering has this advantage, it is important to estimate the two-dimensional noise PSDs with numerical methods such as the one proposed in Section 4.1 of this thesis.

5.3 ACCURACY IMPROVEMENT WITHOUT NOISE PSD INFORMATION

When noise PSDs are not available, the multiple-input system can not be implemented. The procedure discussed in Section 4.4.2 should be applied. The

first stage of this procedure is to improve the horizontal component measurements using the vertical component measurement. This stage begins with approximating the signal PSDs of T_x and T_y using the measurements of T_z. Then the PSDs of the T_x, T_y measurements are estimated. After that, the improved estimates of T_x and T_y can be obtained with Eq. (4.37). The whole idea is based on the fact that the measurements in the vertical channel are much more accurate than the observations in the horizontal channels and the signals in all of those channels are linearly correlated. Shown in Table 5.5 are the accuracies of the improved T_x and T_y. Comparing Table 5.5 with Table 5.2, we can see that the standard deviations of the errors become half of their previous values. The results have nearly the same accuracy level as the T_z measurements.

Table 5.5: Accuracies of the Horizontal Components Improved with the PSD of Vertical Component Measurements

Gravity Vector Component	Min	Max	Mean	Std. Dev.
T_x (mgal)	-8.3	10.0	-0.27	2.62
T_y (mgal)	-10.5	10.9	0.01	2.95

The second stage of the procedure is to improve the vertical component with the estimations of T_x and T_y from the first stage. As discussed in Section 4.4.2, this is theoretically possible. The statistics shown in Table 5.5 indicate that the same accuracy assumption in the frequency domain least-squares adjustment model Eq.

(4.38) is more or less realistic. As expected, and shown in Table 5.6, accuracy gains for every component have been obtained by combining them with the frequency domain least-squares adjustment technique. Here again, the accuracy gain for the vertical component is much less than the gains for the horizontal components. The reason for this is the same as given in Section 5.2.

Table 5.6: Further Accuracy Improvement With Frequency Domain Least-squares Adjustment

Output Signal	Input Signals	Min	Max	Mean	Std. Dev.
T_z (mgal)	T_z	-8.6	5.5	0.19	2.16
	T_z T_x	-6.5	6.1	-0.06	1.95
	T_z T_y	-6.6	8.0	-0.11	2.04
	T_z T_x T_y	-7.1	7.2	-0.09	1.92
T_x (mgal)	T_x	-8.3	10.0	-0.27	2.62
	T_x T_z	-4.8	4.6	-0.06	1.37
	T_x T_y	-7.0	8.1	-0.09	2.12
	T_x T_z T_y	-5.0	4.6	-0.05	1.31
T_y (mgal)	T_y	-10.5	10.9	0.01	2.95
	T_y T_z	-5.6	5.5	0.02	1.45
	T_y T_x	-8.9	9.1	0.01	2.44
	T_y T_z T_x	-5.1	5.4	0.02	1.40

5.4 COMPARISON OF COMBINATION METHODS

In this section, the two spectral methods, namely the multiple-input single-output system and the frequency domain least-squares adjustment, are compared first. Then, the multiple-input system is compared with least-squares collocation. Due to PC memory limitations and the long computation time associated with collocation, this comparison will be conducted only in the case of single input. All the computations in this section are done under the assumption that measurement noise PSDs are known.

In Table 5.7, the results from the multiple-input system and the least-squares adjustment are shown. Because the least-squares adjustment method requires two or more input signals, there are no results for this method in the single input case. Instead, statistics of the simulated measurement noise are given in bold. It can be seen that, while both methods are very effective in reducing the noise in their outputs, the multiple-input system gives better results than the least-squares adjustment method in all cases. This is because, as seen in the theoretical discussion, the multiple system has two basic functions: first, filtering every input signal, and then, combining them optimally. On the other hand, the least-squares adjustment method only performs the weighted averaging of the input signals in the frequency domain. Hence, the effectiveness of the least-squares adjustment

Table 5.7: Comparison of the Multiple-Input System and Frequency Domain LSA

Output Signal	Input Signals	M-input System			Frequency Domain LSA		
		Min	Max	Std. Dev.	Min	Max	Std. Dev.
T_z (mgal)	T_z	-4.5	4.8	1.28	**-8.6**	**5.5**	**2.16**
	T_z T_x	-4.6	4.4	1.18	-5.7	5.7	1.75
	T_z T_y	-4.8	5.3	1.20	-5.6	6.9	1.84
	T_z T_x T_y	-4.5	4.5	1.14	-5.1	5.4	1.49
T_x (mgal)	T_x	-6.5	6.9	1.81	**-19.4**	**14.8**	**4.96**
	T_x T_z	-3.0	2.8	0.73	-4.1	4.1	1.12
	T_x T_y	-5.6	5.1	1.41	-8.7	7.9	2.32
	T_x T_z T_y	-2.7	3.0	0.72	-4.3	3.6	1.02
T_y	T_y	-7.9	6.7	2.02	**-18.0**	**18.5**	**4.81**
	T_y T_z	-3.2	3.3	0.83	-4.5	4.3	1.29
	T_y T_x	-6.8	5.6	1.63	-10.3	12.0	3.41
	T_y T_z T_x	-3.2	3.0	0.81	-4.5	4.0	1.18

method will be very much dependent on whether (or how much) the noise sequences in the input signals are correlated with each other. If they are fully correlated and all the inputs are at same accuracy level, improved results will not be obtained with the least-squares adjustment method. In the case where the input noises are fully correlated and all the inputs are not at the same accuracy level, the accuracy gain of the final result will be due only to the inputs with higher accuracies because the random phase property of noise can not be used. However, better results can always be expected with the multiple-input system due to its filtering function.

From Table 5.7, we also see smaller improvement in T_z and larger improvement T_x and T_y from the least-squares adjustment method, especially when T_z is used as an input. These are again due to the higher accuracy of T_z measurements and the relations between the vertical component and the horizontal components of the gravity disturbance vector as discussed in the previous section of this chapter.

To compare the multiple-input system with least squares collocation, results for all components in the single input case are also computed with collocation. Obviously, collocation can not use all the data. Only the data in the 40 km x 40 km sub-area around the computation point are used. However, the empirical covariances for signals and noise are estimated by employing the data in the whole area. The size of the sub-area is determined by the correlation length of the

vertical component. From Figure 5.12, we can see that the applied sub-area size is selected as a little bit larger than twice the correlation length.

Table 5.8 shows the accuracies of results from both the multiple-input system and least-squares collocation. We can see that they are comparable. Collocation gives less accurate results because only the data in the small sub-area were used. On the other hand, because the correlation length is very short, see Figure 12, the error committed by using data in the sub-area only is probably very small.

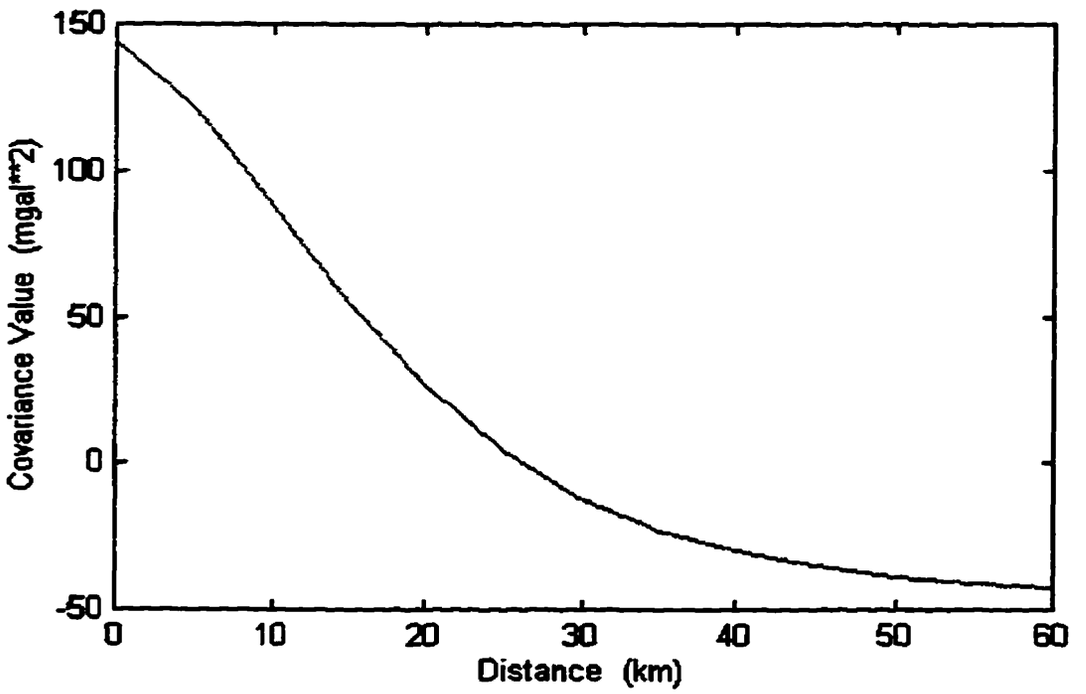

Figure 5.12: The empirical covariance function of the vertical component T_z

Table 5.8: Comparison of the Multiple-Input system and Least-Squares Collocation in the Case of a Single Input Signal

Gravity Vector Component	Multiple-Input System			Collocation		
	Min	Max	σ	Min	Max	σ
T_z (mgal)	-4.5	4.8	1.28	-6.5	6.1	1.76
T_x (mgal)	-6.5	6.9	1.81	-16.2	12.4	2.52
T_y (mgal)	-7.9	6.7	2.02	-16.2	10.9	2.99

5.5 DOWNWARD CONTINUATION OF AIRBORNE GRAVITY DATA

There are two subsections in this section. Subsection 1 shows the results of the downward continuation from one level surface to another. Spectral methods are used to examine the effects of different input combinations on the noise control in downward continuation. In Subsection 2, the use of spectral methods in the downward continuation of airborne gravimetry data to the Earth's natural surface is tested. Results from the spectral method and collocation are compared.

5.5.1 Downward Continuation of Airborne Data to a Level Surface

The downward continuation of airborne gravity data from flight level to another level surface is simple. As discussed in Chapter 4, this function can be built into the multiple-input system and the frequency domain least-squares adjustment program. Thus, the height effect and the input combination effect in downward continuation can be readily examined at the same time. Three flight heights, namely, 500, 1000, and 1500 meter, were chosen for the numerical tests. Noises are the same as used before. Two situations are considered. In situation (a), the noise PSDs are known. In situation (b), the noise PSDs are not known.

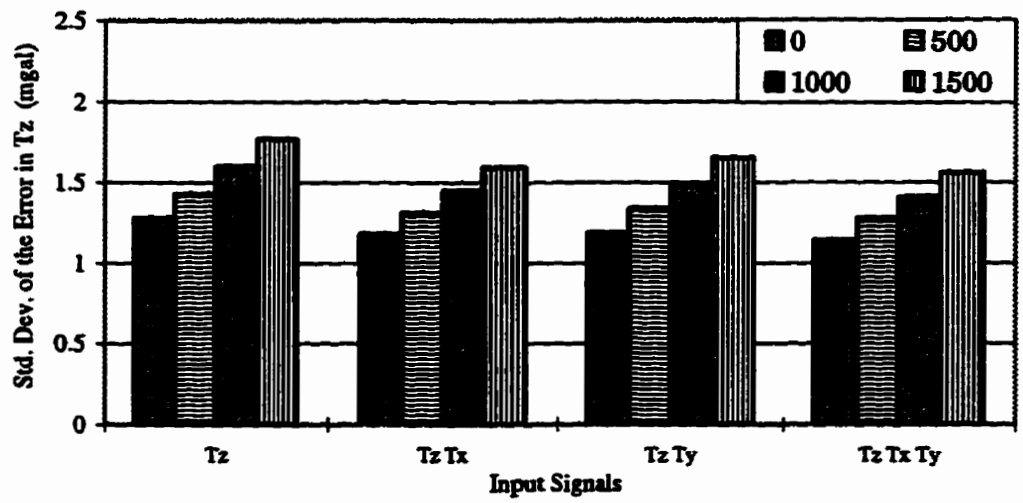

Figure 5.13: The effects of downward continuation height and input data type combination on the accuracy of T_z (noise PSDs known)

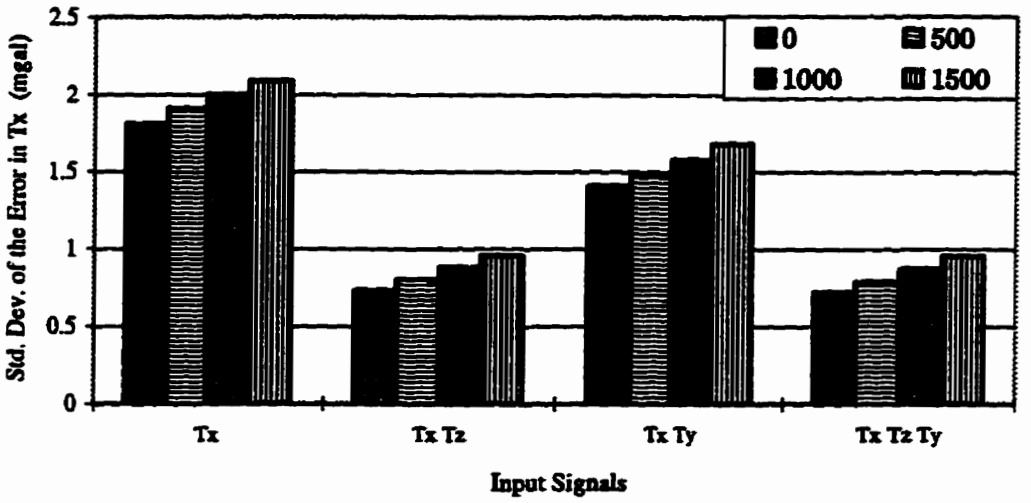

Figure 5.14: The effects of downward continuation height and input data type combination on the accuracy of T_x (noise PSDs known)

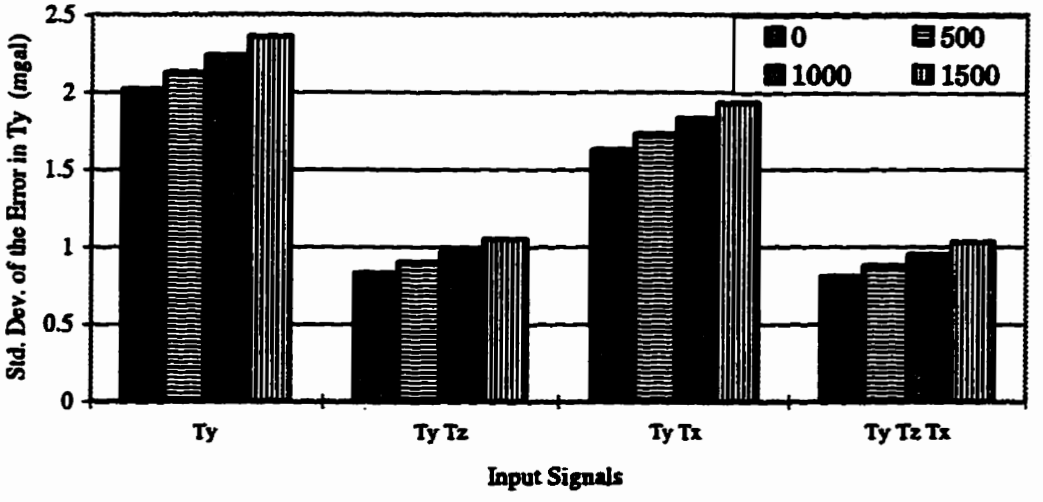

Figure 5.15: The effects of downward continuation height and input data type combination on the accuracy of T_y (noise PSDs known)

Figures 5.13 to 5.15 show the effect of downward continuation as a function of height and the effect of input combination for each component in situation (a). Plotted are error standard deviations of the results versus the height change for each input combination. All the results are computed by the multiple-input system because the PSDs of the input noises are known. According to these figures, we can say that in general, more input signals lead to a more accurate and more stable downward continuation and that the accuracy of the downward continuation decreases as the height increases. Again, as seen in Section 5.2, by involving other components, the improvement in the vertical component is less obvious than those for the horizontal components and much more accurate results can be obtained for the horizontal components when the observations of the vertical component are used. The reason for this is same as given before.

For situation (b), in which the noise PSDs are not known, a two stage procedure should be used in order to get higher accuracy. As we did in Section 5.3 and discussed in Section 4.4.2, in the first stage the horizontal components are improved by using the PSDs estimated from the measurements of the vertical component. Then, in the second stage, the combinations are made and the results are downward continued to the zero height surface. Results are shown in Figures 5.16 to 5.18.

From Figures 5.16 to 5.18, the same conclusions can be drawn as from Figures 5.13 to 5.15. By comparing the two situations, we can see that the height effect is weaker in situation (a). That is because the noise is better controlled in two ways: filtering and combination when the noise PSDs are known, and the only way to control noise level is combination when the noise PSDs are not available. In situation (b), a significant improvement can also be seen in the vertical component when horizontal components are involved. That is because the accuracy of the T_z input is relatively low in this case.

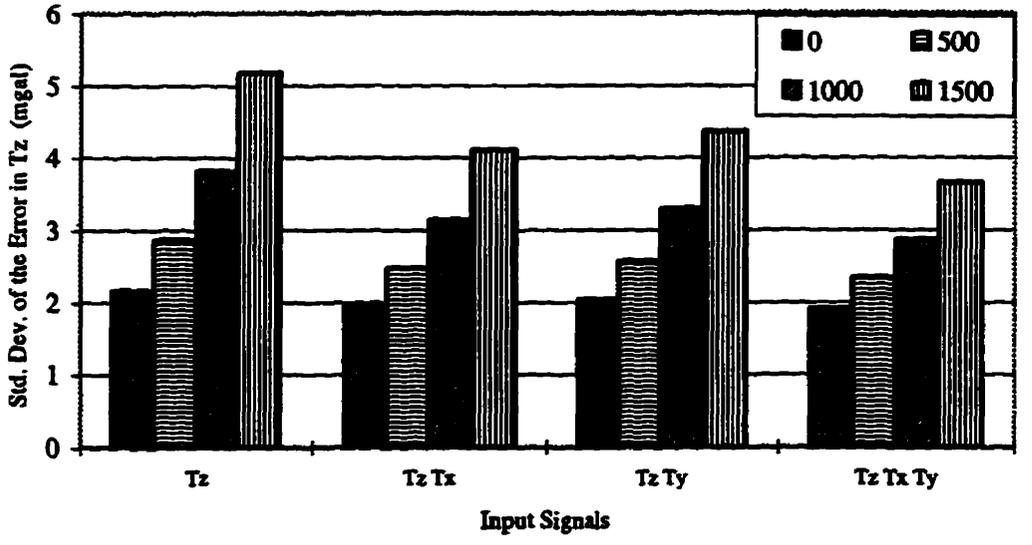

Figure 5.16: The effects of downward continuation height and input data type combination on the accuracy of T_z (noise PSDs unknown)

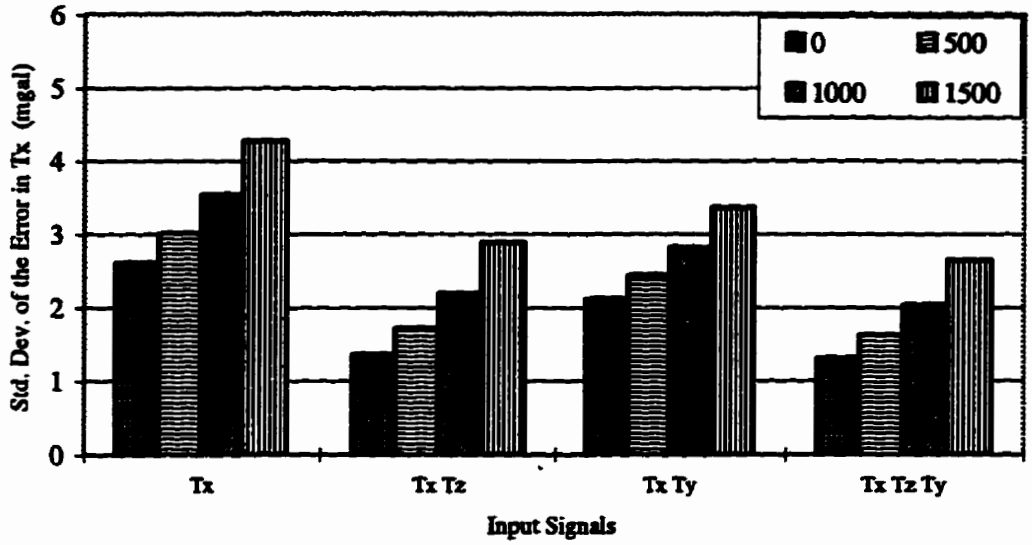

Figure 5.17: The effects of downward continuation height and input data type combination on the accuracy of T_x (noise PSDs unknown)

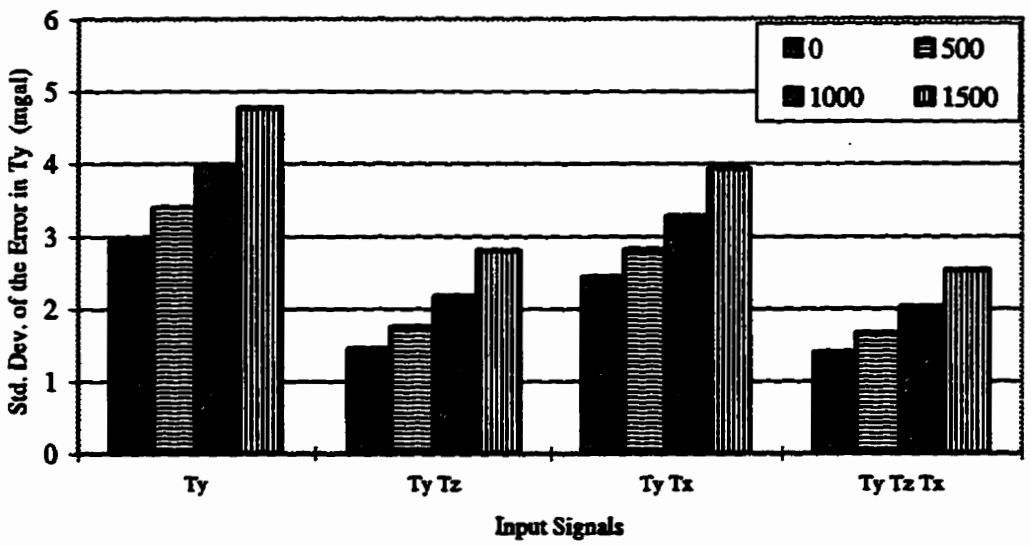

Figure 5.18: The effects of downward continuation height and input data type combination on the accuracy of T_y (noise PSDs unknown)

5.5.2 Downward Continuation of Airborne Data to the Surface of the Earth

These experiments are intended to evaluate the performance of the FFT method for the downward continuation to an arbitrary surface such as the Earth's surface. The arbitrary surface generated for this test is shown in Figure 5.19. It is a rather rugged surface with a height variation from 1000 meters to about 4000 meters. The reference gravity disturbance value at each surface grid point is computed from the point mass model by the integral method. These gravity disturbance values are very accurate and should be considered as error free. The flight level is chosen just above the highest point of the surface with the altitude of 4000 meters. The gravity disturbance at each corresponding grid point is also computed from the point mass model. Because the anomaly masses of the point mass model are buried below the geoid, there is no mass above the geoid. In practice, topographic effect should always have been removed before the downward continuation. It can be done in this case since a digital terrain model must be known in order to conduct such a downward continuation.

The first experiment is designed to test the effectiveness of the FFT method. No noise is added to the components on the flight level surface. Results of the FFT method are compared with results from least-squares collocation. Table 5.9 shows the accuracies of collocation. Again, in the collocation, only the data in

the 40 km x 40 km sub-area around the computation point are used. But this time, the analytical covariance functions need to be employed.

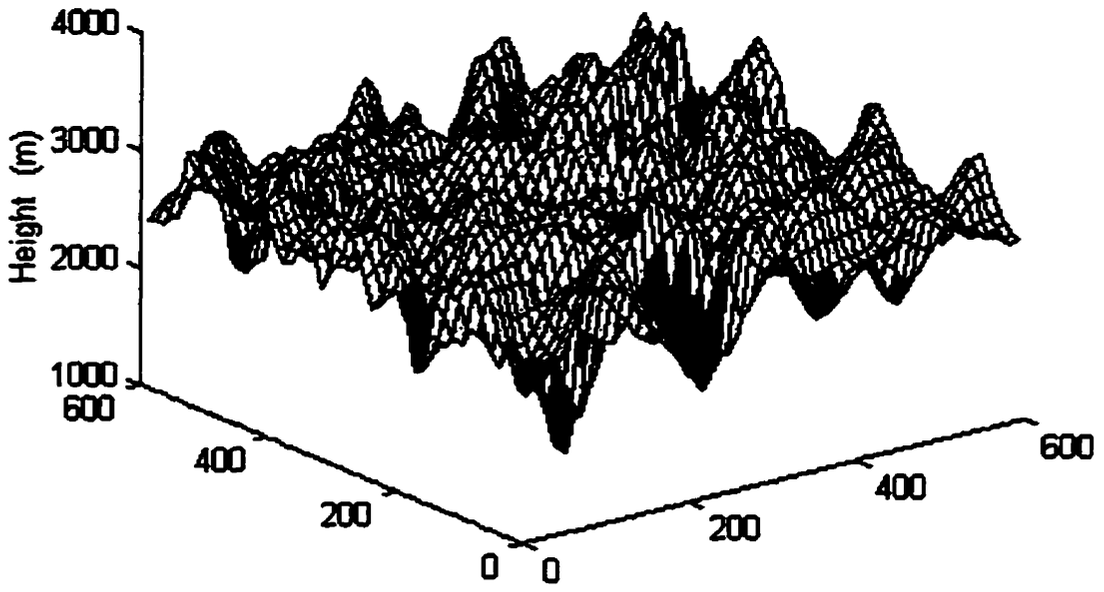

Figure 5.19: The graphic presentation of the generated arbitrary surface

Table 5.9: Accuracy of Downward Continuation With Collocation (noise free)

Gravity Component	Min	Max	Mean	Std. Dev.
T_z	-0.055	0.064	-0.001	0.007
T_x	-0.134	0.099	0.000	0.024
T_y	-0.083	0.095	0.000	0.023

Table 5.10: Accuracy of Downward Continuation With FFT (Noise Free)

Gravity Component	Order of Taylor Series	Min	Max	Mean	Std. Dev.
T_z	1	-0.415	0.761	0.001	0.023
	2	-0.079	0.053	0.000	0.004
	3	-0.027	0.028	0.000	0.003
T_x	1	-0.176	0.272	0.000	0.026
	2	-0.102	0.098	0.000	0.024
	3	-0.102	0.098	0.000	0.024
T_y	1	-0.316	0.351	0.000	0.026
	2	-0.088	0.092	0.000	0.022
	3	-0.088	0.092	0.000	0.022

The results from the FFT method are listed in Table 5.10. As discussed in chapter 3, the FFT method is based on a Taylor expansion. The results for different series of order up to 3 are given in the table to see the effect of the expansion order. As can be seen, both methods are very accurate. The standard deviation of the numerical errors is less than 0.05 mgal. This small number for the collocation

may be due to a number of factors such as the limited amount of data used, the bias in the covariance functions, etc. The FFT method also has the same error sources, but the results are still accurate enough to indicate the effect of the order used in the Taylor expansion. Basically, the higher the expansion order used, the more accurate the results obtained. The extent of the improvement will depend on the high frequency content of the gravity field. However, this is true only in the noise free case. When noise exists, the higher order derivatives in Taylor expansion will also amplify high frequency noises.

To see how sensitive the methods are to noise, simulated noise is added to the vertical component and then the downward continuations with both collocation and the FFT method are conducted. Again, for the FFT method, the order of the Taylor series is chosen to be 1, 2, and then 3 respectively. Table 5.11 shows the results when the noise covariance or PSD function is not used in collocation and the FFT method to do the noise filtering, i.e., pure downward continuation. Table 5.12 gives the results for the case that noise filtering is invovled in the downward continuation. Noises in the results of different methods for the pure downward continuation are illustrated in Figures 5.20 to 5.22 to give an intuitive comparison.

Table 5.11: Comparison of FFT and Collocation in Downward Continuation of T_z When Noise Exists (Filter Not Applied)

Method	Order of Taylor Series	Min	Max	Mean	Std. Dev.
Collocation		**-14.387**	**15.935**	**-0.129**	**4.895**
FFT	1	-8.840	11.030	-0.137	3.761
	2	-11.340	13.900	-0.117	4.454
	3	-12.90	15.050	-0.115	4.678

Table 5.12: Comparison of FFT and Collocation in Downward Continuation of T_z When Noise Exists (Filter Applied)

Method	Order of Taylor Series	Min	Max	Mean	Std. Dev.
Collocation		**-12.981**	**11.975**	**-0.143**	**3.051**
FFT	1	-7.520	7.870	-0.014	2.057
	2	-8.550	9.630	0.003	2.317
	3	-8.820	10.350	0.004	2.396

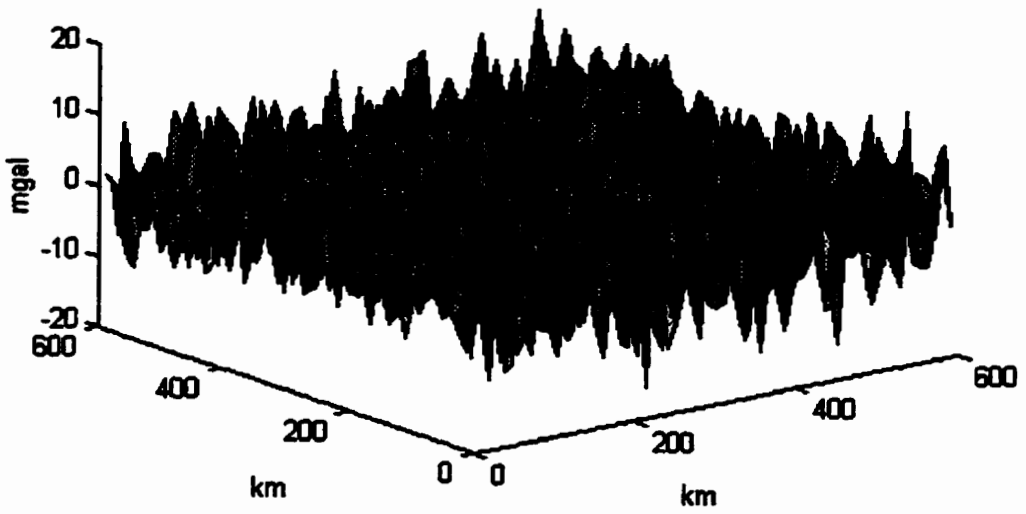

Figure 5.20: Noise in T_z after the downward continuation using collocation

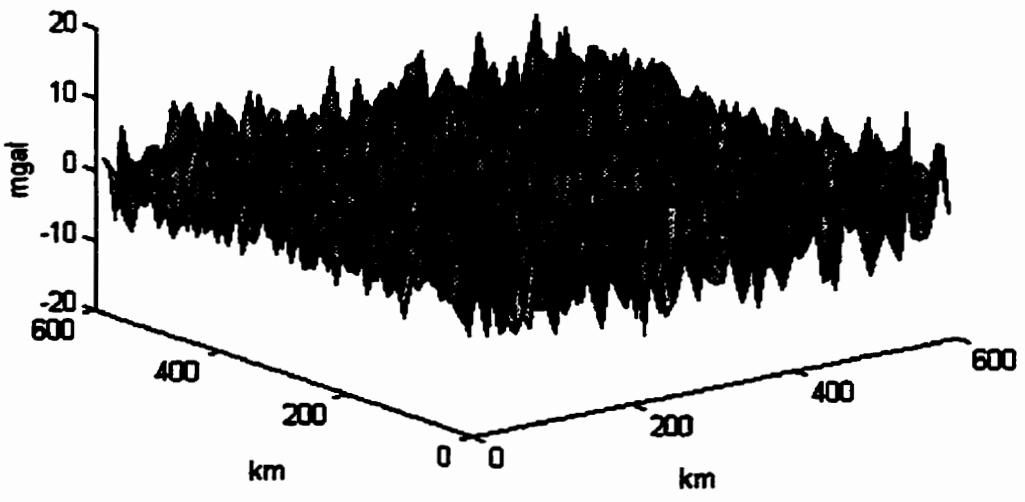

Figure 5.21: Noise in T_z after the downward continuation using the FFT method with 1st order Taylor series

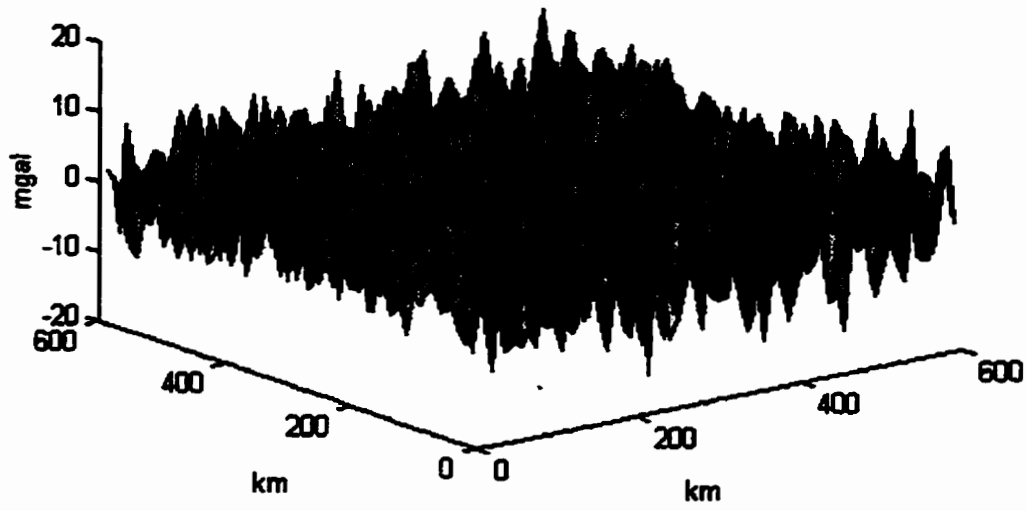

Figure 5.22: Noise in T_z after the downward continuation using the FFT method with 3rd order Taylor series

As shown in Table 5.11, the FFT method is less sensitive to noise and gives more accurate results than collocation. We also see that the FFT method using a higher order Taylor expansion is more sensitive to noise. From Table 5.12, similar conclusion can be drawn. In the mean time, it has been seen in the noise free case that the higher order expansion has a better capability of dealing with high frequency signals. Thus, the higher order terms in Taylor expansion have effects on both high frequency signals and noises.

Nevertheless, the nice thing with the FFT method is that it offers another way to control the noise level, or more precisely, to make a compromise between dealing with very high frequency signals and controlling the noise level. The practical operation for this should be different from location to location according to the roughness of the gravity field. For instance, for the T_z signal used in this research, if we can stand a 0.02 mgal modelling error for the signal and choose a first-order Taylor series, the output noise level will be 0.8 mgal lower compared with the case when the third-order Taylor expansion is used.

5.6 GEOID DETERMINATION USING AIRBORNE VECTOR GRAVIMETRY DATA

Airborne gravimetry has many potential applications in geodesy and geophysics. In geodesy, for instance, geoid determination has been a subject of study for a long time. With the advent of GPS techniques, it has become even more attractive. If the geoid undulation is determined precisely, the orthometric height can be derived by differential GPS instead of spirit leveling. Airborne gravimetry provides a very efficient tool for the acquisition of local high resolution gravity data which is crucial to precise geoid computation.

The multiple-input single-output system is used to compute the local geoid with simulated airborne vector gravimetry data. The goal of this test is to investigate how precise the geoid would be in the wavelength range from 10 km to 100 km and how the two horizontal components would influence geoid determination. The flight height is chosen to be 1000 meters. Measurement noise is the same as simulated in Section 5.1 and all the noise PSDs are assumed to be known. Because the vertical component T_z is more precisely measured, it is included in every input signal combination. The resulting accuracy for each combination is given in Table 5.13.

Table 5.13 indicates that, under the above assumption, the relative geoid in the wavelength range from 10 km to 100 km as determined from airborne gravity data is within a one cm level of accuracy. Combining either one or both of the horizontal components with the vertical component cannot help to give better accuracy and may even make the results worse. This is due to the higher low frequency energy in their noise. Figure 5.23 shows the errors in the geoid determined by using T_z alone. Figure 5.24 shows the error in the geoid computed by combining T_z with T_x and T_y. By comparing these two figures, we can see more variation in the inner area and bigger peaks in the border area in Figure 5.24 than in Figure 5.23, indicating bigger low frequency errors in the geoid computed by combining T_z with T_x and T_y. Thus, scalar gravimetry should be used for geoid determination.

Table 5.13: Accuracies of the Geoid Determined With the Multiple-Input System Using Different Input Combinations, in metres

Output Signal	Input Signals	Min	Max	Mean	Std. Dev.
ζ (m)	T_z	-0.020	0.019	0.000	0.005
	T_z T_x	-0.024	0.026	0.000	0.007
	T_z T_y	-0.033	0.026	0.000	0.008
	T_z T_x T_y	-0.024	0.021	0.000	0.006

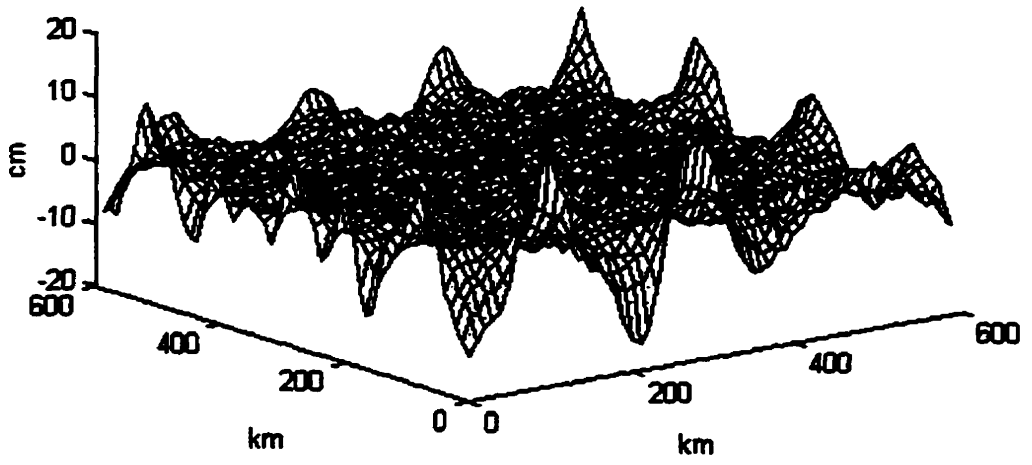

Figure 5.23: Error in the geoid determined by using T_z alone

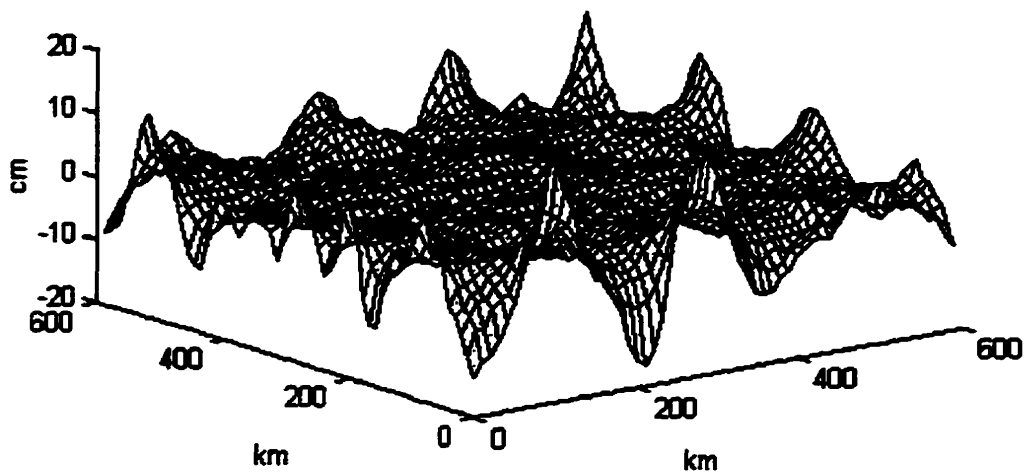

Figure 5.24: Error in the geoid determined by combining T_z, T_x, and T_y

5.7 EFFECT OF GRAVITY FIELD ON FILTERING RESULTS

Tests in this section are given to investigate the impact of the roughness of the gravity field on spectral methods. In addtion to the gravity field (Field #2 in following tables) used in preceeding test, two other local gravity field are simulated. As shown in Table 5.14, Field #1 is much more rugged than the gravity field used before (Field #2) and Field #3 is significantly smoother than Field #2. Noise for all the components remain the same.

Table 5.14: Statistics of the Three Simulated Local Gravity Fields

Gravity Component	Field #1			Field #2			Field #3		
	Min	Max	σ	Min	Max	σ	Min	Max	σ
T_z	-89.6	157.3	19.62	-54.2	88.0	11.99	-24.3	25.8	5.57
T_x	-88.4	73.3	11.67	-53.5	38.6	7.68	-17.2	14.0	3.73
T_y	-129.8	98.0	14.14	-74.3	51.7	9.08	-24.9	16.7	4.13

Table 5.15: Comparison of Accuracies of Wiener Filtering results

Gravity Component	Field #1			Field #2			Field #3		
	Min	Max	σ	Min	Max	σ	Min	Max	σ
T_z	-5.9	7.0	1.89	-4.5	4.8	1.28	-2.2	1.7	0.53
T_x	-8.6	10.5	2.57	-6.5	6.9	1.81	-3.5	3.3	0.86
T_y	-10.8	10.6	3.03	-7.9	6.7	2.02	-3.2	2.9	0.87

As indicated in the theoretical discussion, a multiple-input single-output system first uses Wiener filters to filter each input data set and then combines all the filtered results to obtain the system output. Table 5.15 compares the accuracies of the Wiener filtering results. It is seen that the roughness of the gravity field has a strong effect on the Wiener filtering results. The more rugged the gravity field is, the less accurate are the Wiener

filter results. In all cases, Field #3 has the best results. The reason can be seen from the frequency response of a Wiener filter. When the signal to noise ratio is larger, corresponding to the case of more rugged gravity field, Wiener filter gives more confidence for the input data set so that its effectiveness in reducing noises in the input data set will be affected. Table 5.16 shows the accuracies for all fields obtained from multiple-input single-output system. All three components of each field are used as inputs. As expected, the noise is further reduced. But still, the more rugged field obtains the less accurate results.

Table 5.16: Comparison of Accuracies of Results From Multiple-Input System

Gravity Component	Field #1			Field #2			Field #3		
	Min	Max	σ	Min	Max	σ	Min	Max	σ
T_z	-5.1	6.3	1.64	-4.5	4.5	1.15	-2.2	1.4	0.50
T_x	-8.3	8.1	1.80	-2.7	3.0	0.72	-1.3	1.3	0.37
T_y	-12.3	11.9	2.55	-3.3	3.0	0.81	-1.5	1.4	0.34

Frequency domain least-squares adjustment method is also applied to the three different fields. The obtained accuracies are shown in Table 5.17. The effect of the gravity field roughness can clearly be seen. The same conclusion as in the input-output system case can be drawn here. The reason can be that the stronger gravity field signal (in more

rugged gravity field) would make correlation between input data sets stronger so that the effectiveness of the least-squares adjustment is reduced.

Table 5.17: Comparison of Accuracies of Results From Frequency Domain LSA

Gravity Component	Field #1			Field #2			Field #3		
	Min	Max	σ	Min	Max	σ	Min	Max	σ
T_z	-5.8	6.9	1.72	-5.1	5.4	1.50	-4.6	5.5	1.42
T_x	-9.7	8.5	1.97	-4.3	3.5	1.03	-3.5	3.2	0.95
T_y	-12.4	11.2	2.66	-4.5	4.0	1.18	-3.6	3.7	1.06

Noise level of input data sets will certainly affect the results of spectral methods. To see that, first, three different noise sets are added to the vertical component T_z of Field #2. Then, the Wiener filter is applied to the three obtained data sets. Accuracies of the results are compared in Table 5.18. As expected, higher noise level for a certain gravity field will cause less accurate results.

Table 5.18: Effect of Noise Level on Wiener Filtering Results

Noise in T_z	Noise Level #1			Noise Level #2			Noise Level #3		
	Min	Max	σ	Min	Max	σ	Min	Max	σ
Before Filtering	-17.2	11	4.34	-8.6	5.5	2.17	-4.3	2.75	1.09
After Filtering	-6.8	7.9	1.91	-4.5	4.8	1.28	-2.8	3.1	0.79

CHAPTER 6

CONCLUSIONS AND RECOMMENDATIONS

The advantage of FFT based spectral techniques over other techniques is their computational efficiency. This thesis deals with the use of spectral methods for the post processing of airborne vector gravity data. In general, two aspects of post processing airborne vector gravity data have been discussed: 1) the filtering and combination of airborne measurements to improve their accuracies; 2) the downward continuation of airborne gravity data. Based on the theoretical discussions and the experimental results presented in this paper, the following conclusions can be drawn:

1. The multiple-input single-output system as well as the frequency domain least-squares adjustment method can be implemented using a stepwise procedure so that they will allow the combination of as many input signals as required with a constant amount of computer memory.

2. When measurement noise PSDs are available, both spectral methods discussed in this thesis can be used to combine the observations of different components to obtain better accuracies. Because the multiple-input single-output system possesses both filtering and optimal combination functions, it usually yields more accurate results than the frequency domain least-squares adjustment method which only averages the spectra from the input signals according to the weights determined from their noise PSDs.

3. When measurement noise PSDs are not available, using the measurements of the vertical component to approximately estimate the PSDs of the horizontal component signals and then using Wiener filtering techniques can bring the noise level in the horizontal component measurements down to the same noise level as in the vertical component measurements. Better accuracy for the vertical component and further improvements for the horizontal components can be achieved by combining the vertical component with the previously improved horizontal components using the frequency domain least-squares adjustment techniques. The multiple-input single-output system cannot be implemented without noise PSD information.

4. Using two-dimensional filtering has been proven to be more effective in reducing the measurement noise than using one-dimensional filtering. Thus, it is recommended that two-dimensional noise PSDs be estimated and two-dimensional filtering be used whenever practically possible.

5. Usually, only one-dimensional noise PSDs for airborne vector gravimetry can be obtained through system calibration and analysis. Generally speaking, there is no analytical way to derive a two-dimensional PSD from its one-dimensional counterpart. Numerical tests in this thesis have shown that the form of two-dimensional PSDs for airborne gravimetry are strongly affected by the flight route patterns. The method for obtaining two-dimensional PSDs from one-dimensional PSDs used in this research should also be suitable for practical use.

6. Downward continuation of an airborne gravity component from one level surface to another is as simple as multiplying the Fourier transform of the component by an exponential function in the frequency domain. Thus, the function can be very easily built into any spectral data processing method for airborne gravimetry.

7. Introducing a Taylor series expansion will allow the use of spectral methods for the downward continuation of airborne gravimetry data to an arbitrary surface, e.g., the Earth's surface, with high computational efficiency. This method does not need prior information about the gravity field. Besides, the spectral method provides an additional way to control the amplification of high frequency noise.

8. In the downward continuation of airborne gravity data, more stable and accurate results for every component can be expected when it is combined with other components, especially for the horizontal components when the vertical component is involved in their downward continuations. This conclusion applies both when noise PSDs are available and when they are unavailable.

9. According to the limited tests presented here, using the vertical component of the airborne gravity vector alone, the resultant gravimetric geoid could have an accuracy of better than 1 cm in the wavelength range from 10 km to 100 km, for a gravity field with moderate variations. Combining the horizontal components with the vertical component rather than using the vertical component alone would not improve the geoid results due to the higher low frequency noise in the horizontal channels of

airborne gravimetry. Hence, for geoid determination, the use of scalar gravimetry is recommended.

10. The roughness of gravity field does have an impact on the results of the spectral filtering and combination methods. The numerical tests indicate that noise is more effectively reduced when the gravity field is smoother. Thus, it is suggested that the remove-restore technique be used to remove the signal contents which are known or can be computed with good accuracy from other data sources, e.g., topographic effects, from the measurements before filtering and combination and restore it afterwards.

11. With the capability to deal with large amount of data efficiently, spectral methods are also suitable for processing and combining data from different observation techniques(e.g., terrestrial observation, gradiometry, altimetry) on different level surfaces. Further research on this issue is recommended.

12. Since data used in this research is restricted in the wavelength range of 10 km to 100 km, problems caused by constant biases and linear error trends in observations have not been considered. Numerical investigation on this aspect is suggested.

BIBLIOGRAPHY AND REFERENCES

Adler, R. J., 1981, The Geometry of random fields. J. Wiley & Sons, New York.

Barzaghi, R., A. Fermi, S. Tarantola, and F. Sansò, 1993, Spectral techniques in inverse Stokes and overdetermined problems. Surveys in Geophysics, Vol. 14, No. 4-5.

Bendat, J. S. and A. G. Piersol, 1986, Random data: Analysis and measurement procedures. Second edition, John Wily & Sons, New York.

Bendat, J. S. and A. G. Piersol, 1980, Engineering applications of correlation and spectral analysis. John Wily & Sons, New York.

Boedecker, G., 1985, Inertial gravimetry in a test network. Paper in K.P. Schwarz (ed.): Proceedings of Inertial Technology for Surveying and Geodesy. Publ. # 60005, Dept. of Surveying Eng., The University of Calgary.

Bracewell, R. N., 1986, The Fourier transform and its applications. Second edition, revised. McGraw-Hill, New York.

Brigham, E. O., 1988, The fast Fourier transform and its applications. Prentice Hall.

Brown, R.G., 1983, Introduction to Random Signal Analysis and Kalman Filtering, John Wiley & Sons.

Brozena, J. M., L. C. Kovacs, and W. R. Roest, 1995, Tectonic structures of the Canada Basin, Arctic Ocean revealed by recent aerogeophysical studies, Part I: Aerogravity observations and interpretation. Proceedings of the IAG Symposium on Airborne Gravity Field Determination at the XXI General Assembly of the IUGG, Boulder, Colorado, USA, July 2-14.

Brozena, J. M. and M. F. Peters, 1988, An airborne gravity study of Eastern North Carolina. Geophysics, Vol. 53, No. 2, pp.245-253.

Brozena, J. M., G. L. Mader, and M. F. Peters, 1989, Interferometric global positioning system: Three-dimensional positioning source for airborne gravimetry. J. of Geophys. Res., Vol. 94, No. B9, pp.12,153-12,162.

Colombo, O., 1990, The role of GPS/INS integration in mapping the Earth's gravity field in the 1990s. Proceedings of IAG International Symposium 107 on Kinematic Systems in Geodesy, Surveying and Remote Sensing, Springer-Verlag, New York.

Eissfeller, B. and P. Spietz, 1989, Shaping filter design for the anomalous gravity field by means of spectral factorization. manuscripta geodaetica, 14, pp.183-192.

Eren, K., 1980, Spectral analysis of Geos-3 altimeter data and frequency domain collocation. Report No. 297, Department of Geodetic Science, The Ohio State University.

Forsberg, R., 1995, Downward continuation of airborne gravity data. Paper presented at the XXI General Assembly of the IUGG, Boulder, Colorado, USA, July 2-14.

Forsberg, R. and J. M. Brozena, 1992, The Greenland airborne gravity project - comparison of airborne and terrestrial gravity data. 7th International Symposium on Geodesy and Physics of the Earth, Potsdom, October.

Forsberg, R., 1987, A new covariance model for inertial gravimetry and gradiometry. Journal of Geophysical Research, Vol. 92, No. B2, pp.1305-1310.

Forsberg, R., A. Vassiliou, K. P. Schwarz, and R. V. C. Wong, 1985, Inertial gravimetry - A comparison of Kalman filtering, smoothing and post-mission adjustment techniques. Paper in K.P. Schwarz (ed.): Proceedings of Inertial Technology for

Surveying and Geodesy. Publ. # 60005, Dept. of Surveying Eng., The University of Calgary.

Forsberg, R., 1984, Local covariance functions and density distributions. Report No. 356, Department of Geodetic Science, The Ohio State University.

Gelb, A. (ed.), 1974, Applied optimal estimation. The M.I.T. Press, Cambridge, Mass.

Gerber, M. A., 1978, Gravity gradiometry. Astronautics & Aeronautics, May 1978, pp 18-26.

Gray, R. M., 1977, Toeplitz and circulant matrices II. Information System Laboratory, Technical Report No. 6504-1, Stanford Electronics Laboratories, Stanford University.

Halliday, M. E. and E. E. Klingele, 1995, Airborne gravity survey of Switzerland. Proceedings of the IAG Symposium on Airborne Gravity Field Determination at the XXI General Assembly of the IUGG, Boulder, Colorado, USA, July 2-14.

Hein, G. W., 1995, Progress in airborne gravimetry: solved, open and critical problems. Proceedings of the IAG Symposium on Airborne Gravity Field Determination at the XXI General Assembly of the IUGG, Boulder, Colorado, USA, July 2-14.

Hein, G. W., G. Baustert, B. Eissfeller, and H. Landau, 1988, High precision kinematic GPS differential positioning: Experiences, results, integration of GPS with a ring laser strapdown inertial system. Paper presented at the Int. ION GPS-88, Colorado Springs, Sept. 19-23.

Heiskanen, W. A. and H. Moritz 1967, Physical geodesy. W.H. Freeman, San Francisco, London.

Heller, W. G. and S. K. Jordan, 1979, Attenuated white noise statistical gravity model. Journal of Geophysical Research, Vol. 84, No. B9, pp.4680-4688.

Heller, W. G., K. S. Tait, S. W. Thomas, 1977, GEOFAST — A fast gravimetric estimation algorithm. The Analytic Sciences Corporation.

Huddle, J. R., 1989, Advances in strapdown systems for geodetic applications. Paper in K. Linkwitz and U. Hangleiter (eds.): High Precision Navigation. Springer, Heidelberg.

Huddle, J. R., 1978, Theory and performance for position and gravity survey with an inertial system. J. Guidance and Control, Vol. I, No. 3, pp.183-188.

Huddle, J. R., 1977, The theoretical principles for design of the inertial surveyor for position and gravity determinations. Paper in Proceedings of the 1st Int. Symp. on Inertial Technology for Surveying and Geodesy, Ottawa, pp.45-59.

Jekeli, C. 1984, Analysis of airborne gravity gradiometer survey accuracy. manuscripta geodaetica, Vol. 9, No. 4, pp.323-379.

Jones, P. C. and A. C. Jonhson, Airborne gravity survey in Southern Palmer Land, Antarctica. Proceedings of the IAG Symposium on Airborne Gravity Field Determination at the XXI General Assembly of the IUGG, Boulder, Colorado, USA, July 2-14.

Jordan, S. K. and J. L. Center, 1986, Establishing requirements for gravity surveys for very accurate inertial navigation. Navigation, Vol. 33, No. 2, pp.90-108.

Jordan, S. K. and W. G. Heller, 1978, Upward continuation of gravity disturbance covariance functions. Journal of Geophysical Research, Vol. 83, No. B7, pp.3382-3388.

Jordan, S. K., 1977 Self-consistent statistical model for gravity anomaly, vertical deflection, and undulation of the geoid. Journal of Geophysical Research, Vol. 77, No. 20, pp.3660-3670.

Kasper, J., 1971, A second-order Markov gravity anomaly model. Journal of Geophysical Research, Vol. 76, No. 32, pp.7844-7849.

Keller, W., 1995, Harmonic downward continuation using a Haar wavelet frame. Paper presented at the XXI General Assembly of the IUGG, Boulder, Colorado, USA, July 2-14.

Kleusberg, A., A. Goodacre, and R. J. Beach, 1989, On the use of GPS for airborne gravimetry. Paper presented at the 5th Int. Geod. Symp. on Satellite Positioning, Las Gruces, New Mexico, March 13-17.

Knickmeyer, E. T., 1990, Vector gravimetry by a combination of inertial and GPS satellite measurements. UCSE Report #20035, Department of Geomatics Engineering, The University of Calgary.

Lewis, F.L., 1986, Optimal Estimation With an introduction to stochastic control theory. John Wiley & Sons.

Li, J. and M. G. Sideris, 1995, Marine gravity and geoid determination by optimal combination of satellite altimetry and shipborne gravimetry data. Paper presented at the XXI General Assembly of the IUGG, Boulder, Colorado, USA, July 2-14.

Marple, S. L., 1987, Digital spectral analysis with applications. Prentice Hall, Englwood Cliffs.

Meissl, P., 1967, Probabillistic error analysis of airborne gravimetry. Report No. 138, Dept. of Geodetic Science, The Ohio State University.

Miller, K. S., 1980, An introduction to vector stochastic process. Robert. E. Krieger Publ., New York.

Moritz, H, 1980, Advanced physical geodesy. H. Wichmann Verlag, Karlsruhe, Germany.

Sansò, F. and M. G. Sideris, 1995, On the similarities and differences between systems theory and Least-Squares Collocation in physical geodesy. Paper presented at the XXI General Assembly of the IUGG, Boulder, Colorado, USA, July 2-14.

Sansò, F. and G. Sona, 1995, The theory of optimal linear estimation for continuous fields of measurements. Manuscripta Geodaetica, Vol. 20, No. 3.

Schuster, S. A., 1900, The periodogram of magnetic declination as obtained from the records of the Greenwich Observatory during the Years 1871-1895, Trans. Cambridge Philos. Soc., Vol. 18, pp. 107-135.

Schwarz, K. P., 1973, Investigations on the downward continuation of aerial gravity data, Report No. 204, Department of Geodetic Science, The Ohio State University.

Schwarz, K. P., 1976, Geodetic accuracies obtainable from measurements of first and second order gravitational gradients, Report No. 242, Department of Geodetic Science, The Ohio State University.

Schwarz, K. P. and M. Wei, 1994, Some unsolved problems in airborne gravimetry. Paper presented at the symposium 'Gravity and Geoid', Graz, Austria, September 11-17.

Schwarz, K. P., Y. Li, and M. Wei, 1994, The spectral window for airborne gravity and geoid determination. Proceedings of KIS 94, Banff, Canada, August 30-September 2.

Schwarz, K. P., O. Colombo, G. Hein and E. T. Knickmeyer, 1991, Requirements for airborne vector gravimetry. Paper presented at the XX General Assembly of the IUGG, Vienna, Austria, August 11-24

Schwarz, K. P., M. G. Sideris, and R. Forsberg, 1990, The use of FFT techniques in physical geodesy, Geophysical Journal International, Vol. 100, pp. 485-514.

Shaw, L., I. Paul, and P. Henrikson, 1969, Statistical model for the vertical deflection from gravity-anomaly models. Journal of Geophysical Research, Vol. 74, No. 17.

Sideris, M. G., 1996, On the use of heterogeneous noisy data in spectral gravity field modeling methods. Journal of Geodesy, Vol. 70, No. 8.

Sideris, M. G. and I. N. tziavos, 1988, FFT-evolution and applications of gravity-field convolution integrals with mean and point data, Bull. Geod., Vol. 62, pp.521-540.

Sideris, M. G., 1987, Spectral methods for the numerical solution of Molodensky's problem. UCSE Report #20024, Department of Geomatics Engineering, The University of Calgary.

Sideris, M. G., 1987, On the application of spectral techniques to the gravimetric problem. Proceedings of the XIX IUGG General Assembly, Tome II, Vancouver, B.C., August 9-22.

Sideris, M. G., 1984, Computation of gravimetric terrain corrections using fast Fourier transform techniques. UCSE Report #20007, Department of Geomatics Engineering, The University of Calgary.

Smith, J. M., 1987, Mathemeatical modelling and digital simulation for engineering and scientist, second edition. John Wiley & Sons.

Sunkel, H., 1984, Splines: Their equivalence to collocation. Report No. 357, Dept. of Geodetic Science, The Ohio State University.

Tziavos, I. N., M. G. Sideris, and K. P. Schwarz, 1992, A study of the contributions of various gravimetric data types on the estimation of gravity field parameters in the mountains. Journal of Geophysical Research, Vol. 97, No. B6, pp.8843-8852.

Vassiliou, A. A. and K. P. Schwarz, 1987, Study of the high frequency spectrum of the anomalous gravity potential. Journal of Geophysical Research, Vol. 92, No. B1, pp.609-617.

Vassiliou, A. A., 1986, Numerical techniques for processing airborne gradiometer data. Ph. D. thesis, Department of Geomatics Engineering, The University of Calgary.

Wei, M. and K.P. Schwarz, 1994, An error analysis of airborne vector gravimetry. Proceedings of KIS 94, Banff, Canada, August 30-September 2.

Wei, M., S. Ferguson and K. P. Schwarz, 1991, Accuracy of GPS-derived acceleration from moving platform tests. Paper presented at the XX General Assembly of the IUGG, Vienna, Austria, August 11-24.

Wiener, N., 1949, Extrapolation, interpolation and smoothing of stationary time series, with engineering applications. Wiley, New York.

Wu, L. and M. G. Sideris, 1995, Using multiple input-single output system relationships in post processing of airborne gravity vector data. Proceedings of the IAG Symposium on Airborne Gravity Field Determination at the XXI General Assembly of the IUGG, Boulder, Colorado, USA, July 2-14.